

**16 INCH COMPOSITE MATERIAL TELESCOPE WITH ADAPTIVE
OPTICS.**

**KEY COMPONENTS: WAVEFRONT RECONSTRUCTOR &
VIBRATION TESTING**

By

Freddie Santiago,.

A thesis submitted in partial fulfillment of the requirements for the degree of

MASTER OF SCIENCE

in

PHYSICS

UNIVERSITY OF PUERTO RICO
MAYAGÜEZ CAMPUS

December, 2006

Approved by:

Héctor J. Jiménez, Ph.D
Member, Graduate Committee

Date

Erick Roura, Ph.D
Member, Graduate Committee

Date

Mark Chang, Ph.D
President, Graduate Committee

Date

Paul Castillo, Ph.D
Representative of Graduate Studies

Date

Héctor J. Jiménez, Ph.D
Chairperson of the Department

Date

©2006, Freddie Santiago .:

Dedication

I dedicate this thesis first to the Great Architect of the Universe, to my mother, Cruz E. Fernández, to my father, Freddie Santiago, to my brother Wilfredo Santiago, to Orion, to my cousins, to the Fernández and Santiago family in PR, to the Restaino and Yeppa family in NM and to all my friends which made this work possible by their constant support.

To the memory of Christopher Restaino.

Acknowledgments

I would like to thank those involved in ensuring the completion of this thesis project. I would like to thank my advisors Dr. Mark Chang, Dr. Hector Jiménez, Dr. Erick Roura, Dr. Pablo Marrero of the Physics Department at the University of Puerto Rico and Dr. Sergio R. Restaino of the Naval Research Laboratory. I also appreciate the assistance of Dr. Ty Martínez of the Naval Research Laboratory and Don Payne of Narrascope, Inc. for their support. Special thanks for Dr. José López for his support through my career and Dr. Erick Roura for been my older brother throughout all these years.

I would also like to thank my colleagues Jonathan R. Andrews, Carlos O. Font, Luis B. Arroyo and Teddy A. Rodríguez for all their help through this entire project. Especially to Christopher Wilcox for the pictures and his mother Claudie Zamet-Wilcox for all their constant support, help and advice. Thanks also to Odalys Michelle Crespo for her emotional support. To Dr. Arturo Portnoy, Dr. Luis F. Cáceres, Alfredo Moreu, Waleska M. Cruz, Heriberto Hernandez, Sadi and Ida Hernández and Edith Ruiz thanks for making this possible in their special way. Special thanks to Michelle, Sergio, Alex Restaino and Pita for adopting me as one of their own and giving me the advice and support I needed for this project and my life.

16 inch Composite Material Telescope

with Adaptive Optics, Key Components: Wavefront Reconstructor & Vibration Testing

by

Freddie Santiago .:

B.S., Theoretical Physics, University of Puerto Rico, 2001

M.S., Physics, University of Puerto Rico, 2006

Abstract

Advances in technology has provided means for astronomical optical telescopes to increase the aperture diameter (more light collecting capability) therefore increasing the resolution. Better resolution allows telescopes to observe more details and fainter objects. But an increase in diameter means an increase in optics size, which needs big and heavy structures to support them. New developments in composite materials have allowed Composite Mirror Application(CMA) in Tucson, Arizona to build a carbon fiber reinforced polymer(CFRP) telescope and optics for the Naval Research Laboratory(NRL), reducing significantly its weight. Other than weight, atmospheric turbulence is the other major problem for an increase in telescope resolution, but technologies such as adaptive optics(AO) can mitigate its effects. AO

refers to systems which can adapt to compensate for effects introduced by the atmosphere or another medium. This thesis presents the results of two studies done on this next-generation telescope. First it presents work done on the development of two wavefront reconstructors for AO systems that the new telescope will use. The two reconstructors are based on Finite Difference(FD) and Finite Element(FE) methods, respectively. Second, work done on the characterization of the vibration behavior for this new type of composite material telescope is presented. Preliminary analysis of the data was performed using a new technique for analysing nonlinear systems, the Empirical Mode Decomposition(EMD). Data for both experiments was obtained from a 16 inch composite material telescope prototype and from a non-conventional AO system Shack-Hartmann wavefront sensor.

Resumen

Avances en la tecnología han provisto los medios para telescopios astronómicos ópticos de manera que puedan aumentar el diámetro de su apertura (aumentando la capacidad de recolectar más luz), aumentando así su resolución. Una mayor resolución permite observar más detalles y objetos menos luminosos. Pero un aumento en diámetro significa un aumento en el tamaño de los componentes ópticos, lo que requiere estructuras más grandes y pesadas. Nuevos desarrollos en materiales compuestos han permitido a Composite Material Application(CMA) en Tucson, Arizona construir un telescopio y sus componentes ópticos de un polímero de carbono reforzado para los Laboratorios de Investigación de la Marina estadounidense (NRL, por sus siglas en ingles), reduciendo así significativamente su peso. Además del peso, la turbulencia atmosférica es el mayor problema cuando se aumenta la resolución de un telescopio, pero tecnologías como la óptica adaptable(OA) pueden ayudar a mitigar estos efectos. OA se refiere a un sistema que se puede adaptar para compensar por los efectos introducidos por la atmósfera u otro medio. Esta tesis presenta los resultados de dos estudios hechos en esta nueva generación de telescopios. Primero se

presenta el trabajo realizado en el desarrollo de dos reconstructores de frente de onda para el sistema de OA que el nuevo telescopio va a utilizar. Los dos reconstructores están basados en los métodos de diferencia finita y elemento finito, respectivamente. El segundo estudio consiste en la caracterización del comportamiento vibratorio de este nuevo tipo de telescopio de material compuesto. Un análisis preliminar de la data fue hecho utilizando una nueva técnica para sistemas no-lineales llamado Descomposición Modal Empírica (DME). La data para ambos experimentos fue obtenida utilizando un telescopio prototipo de material compuesto de 16 pulgadas y un sensor de frente de onda Shack-Hartmann de un sistema de OA no-convencional.

Contents

List of Figures	xii
List of Tables	xvii
1 Introduction	1
1.1 Image formation	2
1.2 Angle of arrival and Image Jitter	5
1.3 Atmospheric Turbulence	6
1.4 Optical telescope Structure	9
1.4.1 Composite material telescope	11
1.4.2 Vibration and flexure effects on imaging	14
1.5 Introduction to Adaptive Optics and Adaptive Tip/Tilt corrector . .	15
1.5.1 Wavefront Sensor	21
2 Wavefront Reconstruction (WFR)	26
2.1 Finite difference overview	26

Contents

2.2	Results for FD	28
2.3	Finite element overview	35
2.4	Results FE	38
3	Comparison between FD and FE	43
4	Vibration testing of a 16” Composite Material Telescope	55
4.1	Background on Vibration Testing	55
4.2	Experimental description and results	58
4.2.1	Data acquisition	62
4.2.2	SDOF fitting analysis and results	67
4.2.3	Empirical Mode Decomposition (EMD)	73
4.2.4	Results	76
5	Conclusions	86
	Appendices	88
A	EMD results for telescope at 45° from zenith	89
	References	97

List of Figures

1.1	Airy pattern for an ideal telescope	3
1.2	Angle of arrival	6
1.3	Atmospheric turbulence	7
1.4	Wavefront propagating through multiple phase screens.	8
1.5	Matlab Simulation of atmospheric turbulence blurr on an image . .	9
1.6	Telescope changes through history	10
1.7	16 inch Optical Telescope Assembly Prototype	12
1.8	OTAP on top of Adaptive Optics box	13
1.9	Aerial view of the Navy Prototype Optical Interferometer (NPOI) .	13
1.10	DM and stage	17
1.11	Sample setup of an AO system, Courtesy of C.C.Wilcox	18
1.12	Adaptive Tip/Tilt mirror:(a)AutoCAD drawing of the optical setup for the DM and Tip/tilt. (b)DM on Tip/tilt stage. Courtesy of C.C.Wilcox	19
1.13	Sample setup of a new technique AO system, Courtesy of C.C.Wilcox	20

List of Figures

1.14	Drawing of a Hartmann Wavefront Sensor	22
1.15	(a)Shack-Hartmann wavefront drawing. (b)Picture of lenslet array. .	23
1.16	(a)SHWFS AutoCAD drawing, plane wavefront and, (b)aberrated wavefront focusing on the receiver's plane. Courtesy of C.C.Wilcox .	24
2.1	Application of the central difference scheme	27
2.2	General dimensions for a FD N X N matrix formation	28
2.3	Adaptive Tip/Tilt	29
2.4	Flat mirror reconstructor steps, FD	31
2.5	Flat mirror reconstructor results with FD	32
2.6	OKO DM unpowered reconstructor results with FD	33
2.7	OKO DM powered reconstructor results with FD	34
2.8	Global and elements nodes	36
2.9	Horizontal path propagation measurements over the sea, HOPA . . .	37
2.10	Flat mirror reconstructor steps, FE	39
2.11	Flat mirror reconstructor results with FE	40
2.12	OKO DM unpowered reconstructor results with FE	41
2.13	OKO DM powered reconstructor results with FE	42
3.1	Flowchart for both of codes methods, FD and FE	46
3.2	GUI created in Matlab for the codes	47
3.3	Selection of the mask from the reference image	47

List of Figures

3.4	Planes normals and average	48
3.5	Normals for flat1 and their respective average in dashed line, FD . .	49
3.6	Normals for OKOunpow and their respective average in dashed line, FD	50
3.7	Normals for OKOpow and their respective average in dashed line, FD	51
3.8	Normals for flat and their respective average in dashed line, FE . . .	52
3.9	Normals for OKOunpow and their respective average in dashed line, FE	53
3.10	Normals for OKOpow and their respective average in dashed line, FE	54
4.1	Single degree of freedom system	56
4.2	Theoretical damped vibration response of a structure	57
4.3	Vibration test experiment	59
4.4	Pendulum weight system	60
4.5	Vibration experiment set-up	61
4.6	Telescope measurements at different angles performed inside	63
4.7	Oscilloscope GUI and output file sample	64
4.8	Signal obtained from the accelerometers	66
4.9	Fitted analytical functions on the signal	68
4.10	Decaying envelope function for both channels	69
4.11	Decaying envelope function for both channels	70

List of Figures

4.12	Power Spectra for CH1	71
4.13	Power Spectra for CH2	72
4.14	Sifting process: signal information	74
4.15	Sifting process: First step	75
4.16	Sifting process: Second step	75
4.17	Sifting process: Third step	76
4.18	IMFs CH1	77
4.19	IMFs CH2	78
4.20	Phase angle plots for CH1.	80
4.21	Amplitude plots for CH1.	81
4.22	Decaying fit made for IMF1 from the telescope at zenith.	82
4.23	Power spectra after EMD for IMF1 from CH1	84
4.24	Power spectra after EMD for IMF1 from CH2	85
A.1	IMF's for CH1 at 45° from zenith	90
A.2	IMF's for CH2 at 45° from zenith	90
A.3	Phase plots for CH1 at 45° from zenith.	91
A.4	Amplitude plots for CH1 at 45° from zenith.	92
A.5	Phase plots for CH2 at 45° from zenith.	93
A.6	Amplitude plots for CH2 at 45° from zenith.	94

List of Figures

A.7	Decaying fit made for the data from the telescope at 45° from zenith, CH1.	95
A.8	Decaying fit made for the data from the telescope at 45° from zenith, CH2.	96

List of Tables

3.1	Approximate calculation of tip and tilt	45
3.2	Percent Difference for the Tilt, θ_{mean} , calculation between the two methods	45
3.3	Execution time for the solution of the linear system	45
4.1	Parameters obtained from Fourier analysis on the data	73
4.2	Parameters obtained from the decaying enveloped fit	83
A.1	Parameters obtained from the decaying enveloped fit	91

Chapter 1

Introduction

Interest in high resolution imaging, atmospheric optics, laser communications, optical interferometry, fast tracking optical systems and many other areas of study today require the use of telescopes as their means of gathering, focusing or transmitting electromagnetic radiation. Each of these fields require telescopes with specific functions, design, size, mobility and optical quality. As an example, laser communications, satellite imaging and optical interferometry require light weight telescopes that can be transported or move easily and have the ability of tracking fast objects in the sky. On the other hand, high resolution imaging, requires good quality optics and larger optical elements.

The resolution of ground-based optical telescopes is affected by aberrations and diffraction effects. These are caused by numerous factors such as the optical quality, finite aperture and structures of the telescope but mainly by atmospheric turbulence. The scientific interest in constructing new instruments and techniques to improve image resolution of telescope keeps growing resulting in our ability to see new things, ranging from the surfaces of individual stars[1] to the centre of our galaxy[2].

This thesis presents the preliminary work performed on key aspects of instrumen-

Chapter 1. Introduction

tation for image formation, specifically for an new technique Adaptive Optics(AO) system and a non-conventional telescope. For the Adaptive Optics system, it was study, specifically the wavefront reconstructor, and for the new technology telescope on the preliminary structure analysis. The main interest is to present techniques and methods on how to measure low order aberrations such as tip and tilt of the wavefront which introduces jitter in the image.

The thesis is organized as follow:

- Chapter 1: Presents a brief introduction to image formation, atmospheric turbulence, adaptive optics and telescope structure vibrations.
- Chapter 2: Describes the background of a wavefront reconstructor based on Finite Difference(FD) and results derived from a Shack-Hartmann wavefront sensor for an actively controlled incident beam. Also, it present a wavefront reconstructor based on a Finite Element (FE) algorithm in order to verify the results from FD.
- Chapter 3: Presents a comparison of the results from FD and FE.
- Chapter 4: Presents the vibration tests performed on the 16" ground breaking technology telescope and subsequent data analysis, via Fourier methods and Empirical Mode Decomposition (EMD).
- Chapter 5: Conclusions.

1.1 Image formation

An imaging system is one which transforms an object light distribution to an image light distribution. It can be said that the image formation process is linear and space

Chapter 1. Introduction

invariant. A linear optical system is one which maps each object point uniquely to a conjugate image point. Therefore, it can be thought of in terms of a system's response(image formation) to a unit impulse(point object).

The Point Spread Function (PSF) for an ideal telescope is the image of a perfect point source at infinity, such as a star; an approximate model of it can be computed as the Fourier transform of the field in the exit pupil of the telescope. For an unaberrated, unobscured telescope this PSF has the well-known form of the Airy pattern, Figure 1.1.

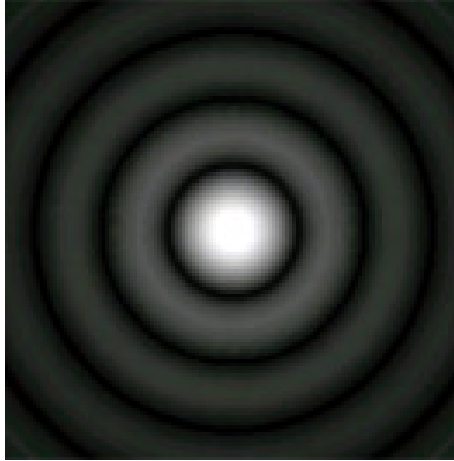


Figure 1.1: Airy pattern for an ideal telescope

Generally the PSF of telescopes is limited by atmospheric turbulence rather than diffraction of the optics. In a general case image formation for a diffraction-limit telescope can be modeled by equation 1.1, as the convolution of the brightness distribution of the object under observation with the telescope point spread function(PSF),

$$U_i(u, v) = \tilde{h}(x, y) \otimes U_g(x, y) \quad (1.1)$$

where $\tilde{h}(x, y)$ is the modified PSF, U_g is the image predicted by geometrical optics and \otimes refers to convolution [3].

Chapter 1. Introduction

Some of the most common degrading factors on the ideal PSF are

- errors on the optics: diffraction, aberrations, misalignment, optical quality, etc
- atmospheric turbulence
- structures of the telescope: diffraction caused by a secondary mirror, aperture stop of the telescope, etc
- mechanical vibration: wind, tracking of motors, ground vibrations, thermal changes, etc

These effects cause the PSF to decrease in amplitude or peak intensity and at the same time increase its width. In other words, these induce aberrations, causing blurring of the images. Some of these limitations are due to physical and there is little that can be done to improve their effects, but others such as aberrations introduced by atmospheric turbulence, optical quality of the telescope and vibration of the structure, can be measured and mitigated.

In 1902, K. Strehl introduced the term, *definition of brightness*, to quantify the performance criteria of optical systems. This quantity is known as the Strehl ratio and can be computed from the PSF by comparing the intensity profile of an image of a point source to the intensity profile it would have if diffraction-limited. In other words it is the ratio between the intensity of a beam on axis with its diffraction limited value. The on-axis intensity, I_0 , is given by

$$I_0 = \frac{\pi^2(D/2)^4}{\lambda^2 L^2} I_{Aper} \quad (1.2)$$

where D is the diameter of the aperture, L is the propagation distance ($L \gg D$), and I_{Aper} is the intensity at the circular aperture. With aberrations the on axis intensity is given by

$$I_0 = S \frac{\pi^2(D/2)^4}{\lambda^2 L^2} I_{Aper} \quad (1.3)$$

Chapter 1. Introduction

where S is the Strehl ratio approximately given by,

$$SR \approx \exp \left[- \left(\frac{2\pi}{\lambda} \right)^2 (\Delta\phi)^2 \right] \quad (1.4)$$

where $(\Delta\phi)^2$ is the wavefront error variance [4].

Sections 1.2, 1.3, and 1.4.2 presents an introduction to image jitter, atmospheric turbulence and structure vibration on imaging systems respectively. Section 1.5 presents a description of adaptive optics(AO), used to correct or mitigate for the effects mentioned previously. The main focus was the wavefront sensing part, specially in wavefront reconstruction techniques.

1.2 Angle of arrival and Image Jitter

The angle of arrival at the receiver of an optical imaging system measures the instantaneous direction of propagation of the wavefront. It is given by the angle subtended between a reference wavefront and the angle of the arriving wavefront, Figure 1.2, This angle, θ , is given by

$$\theta = \frac{\Delta l}{d} \quad (1.5)$$

where Δl is the optical path difference and d is the collecting optics' diameter[5]. The reference wavefront is a known wavefront in which the isoplane lies perpendicular to the optical axis. The Fluctuations in the angle of arrival of the wavefront at the plane of the receiver aperture in the focal plane of the imaging system causes image jitter. This quantity is also known as tilt or dynamic tilt, beacuse it is actually tip and tilt of the wavefront in the receiver plane. The root-mean-square(rms) image displacement is given by the rms of the angle of arrival multiplied by the focal length of the collecting optics,

$$\text{rms}_{id} = \langle \theta^2 \rangle^{1/2} f \quad (1.6)$$

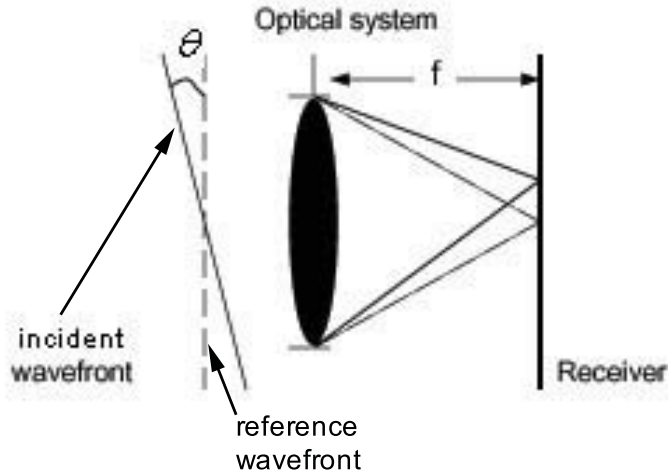


Figure 1.2: Angle of arrival

The rms of the angle of arrival is given by

$$\langle \theta^2 \rangle^{1/2} = \frac{\langle (\Delta S)^2 \rangle}{(kd^2)} \quad (1.7)$$

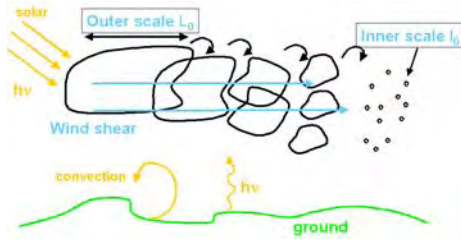
ΔS is the total phase shift across the collecting surface and k is the optical wave number equal to $2\pi/\lambda$, [5]. The two main contributors of jitter in optical telescopes are atmospheric turbulence and telescope structure induced vibrations.

1.3 Atmospheric Turbulence

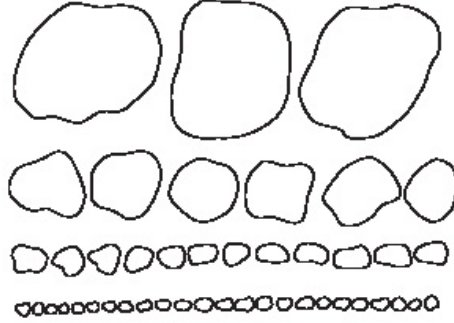
Atmospheric turbulence seriously affects optical systems in which the incident light propagates through long atmospheric paths. It limits the angular resolution of astronomical telescopes at visible and near-infrared wavelengths. The origin of these limitations are the random fluctuations of the index of refraction of the air produced by turbulent air motion. Atmospheric turbulence is generated by the heating and cooling of the Earth's surface, Figure 1.3(a). This diurnal heating and cooling process, produces large scale movement of air masses, which in time become turbulent.

Chapter 1. Introduction

In this large scale movement, large eddies of diameter L_0 , break up into small scale motion, of approximately diameter l_0 , eventually giving rise to randomly distributed pockets of air, each having a characteristic temperature [6], as can be seen in Figures 1.3(b). The range of L_0 is from approximately $\approx 10 \rightarrow 10000m$ and l_0 is below 10m. For example measurements performed at Cerro Paranal, Chile had obtained a mean value for L_0 of 24 m[7]. Since the index of refraction of air is sensitive to



(a) Atmospheric turbulence: Eddies formation process



(b) Scale movement of Eddies from large L_0 to small l_0 scale

Figure 1.3: Atmospheric turbulence

temperature, the atmosphere exhibits random variations in it.

Kolmogorov developed a model of how the energy is transported from the large scale to small scale turbulent eddies[8]. Tatarskii[9] applied Kolmogorov's model to solve the wave equation for propagation in a medium with weak random fluctuations. Fried used Tatarskii's results to derive a useful single parameter r_0 , referred to as the

Chapter 1. Introduction

atmospheric coherence parameter. This is used to describe the effects of turbulence on the resolution of imaging systems. This Fried parameter, also known as the seeing cell size, refers to the statistical quantity which describe the size of this pockets of air described above. This quantity can be interpreted as the aperture size beyond which further increase in diameter results in no further increase in resolution. Light propagating from a distant star forms a plane wavefront at the moment it arrives at the Earth's atmosphere. Figure 1.3 shows an incoming plane wavefront incident on the Earth's atmosphere, resulting in an aberrated wavefront, affecting its amplitude and phase. The consequence is that image resolution is mostly limited by atmospheric

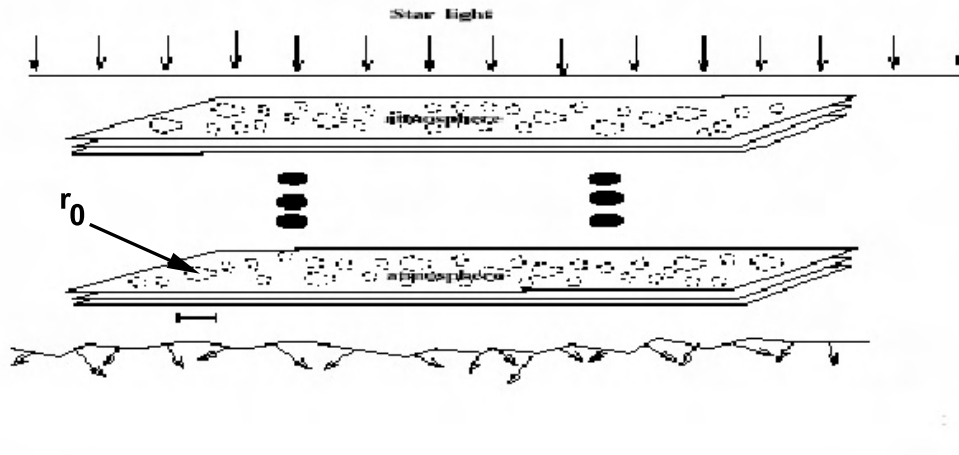


Figure 1.4: Wavefront propagating through multiple phase screens.

turbulence, rather than by the optical quality, design and size of the telescope. Figure 1.5(a) and 1.5(b) shows a simulated situation for the effect of the atmosphere on a star observed through a telescope. A practical interpretation is that a large telescope resolution, is equivalent to that obtained from a much smaller telescope of aperture size of the order of the seeing cell parameter, r_0 . A typical value of r_0 under good seeing conditions range from 10 to 20cm and under bad conditions approximately 5cm [4].

There are various techniques which help mitigate or correct the effects of atmo-

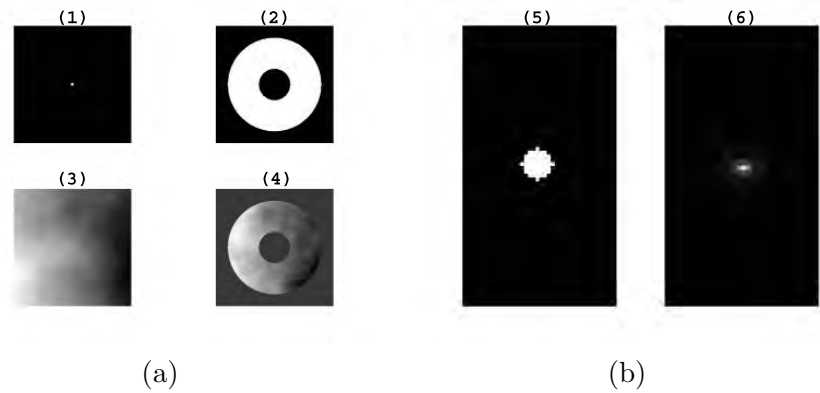


Figure 1.5: Simulation:(a)(1)Point source (2)Typical telescope aperture (3)Turbulence layer (4)Layer and point source as seen through the telescope aperture. (b)(5)Enlarge point source(6)Image of the point source blurred by atmosphere

spheric turbulence,

- pure post-facto techniques
- real-time techniques
- combination of both

Since changes in the atmosphere are approximately of the order of 100 times per second¹, the optical wavefront at the receiver moves very rapidly, and the resulting image seems to "dance" at the receiver plane.

1.4 Optical telescope Structure

Through history one of the main uses for telescopes has been in astronomy. Since the great italian scientist Galileo Galilei's(1564-1642) telescope, Figure 1.6(a), to the

¹This changes are in the visible regime.

Chapter 1. Introduction

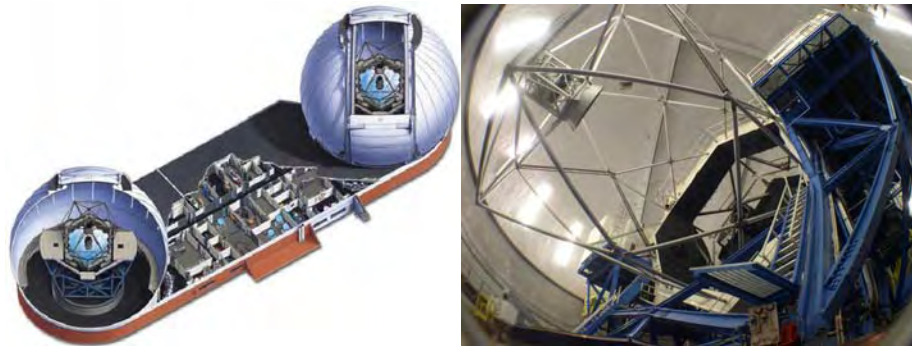
Keck observatory, Figure 1.6(c), science has been pushing the technological envelope to increase the resolution and the collecting capabilities of optical telescopes.



(a) Galileo's Telescope, 1/2" refractor mounted on a wooden rod.



(b) Newton's Telescope, 3" reflector mounted on a brass rotation stage



(c) Keck Telescope, taken from Keck Telescope webpage

Figure 1.6: Telescope changes through history

The main design constraint of ground based optical telescope is the mechanical stability of the primary and secondary mirrors. But there are other engineering limitations such as optical quality and misalignment, structural vibrations, weight, etc. The combination of these constraints affect a telescope's image formation capability.

Chapter 1. Introduction

The need for improved optical telescopes has required increased research on new materials and technologies for the construction and design of support structures for the usually massive optics.

1.4.1 Composite material telescope

The Wavefront Sensing & Control group from the Naval Research Laboratory(NRL) in New Mexico in combination with Composite Mirror Application(CMA) at Tucson, Arizona and a group from the Advanced Composite Materials Laboratory at the University of Northern Arizona(UNA), Flagstaff is working in developing a telescope support structure and optics made entirely of carbon fiber reinforced polymer (CFRP). Carbon fiber are thin filaments made of elementary carbon with structures that vary from those of the amorphous carbon to those of the crystalline graphite. As the carbon density is low, the specific rigidity is very high, three times or more than that of steel. Carbon fiber keep the electric, thermal and chemical characteristics of carbon. CMA has provided NRL with a 16" Optical Telescope Assembly Prototype(OTAP) for optical and structural tests. A necessary step for testing was the construction of a control system. The fork mount of an 8" Celestron telescope was modified to fit this 16" OTAP, as seen in Figure 1.7.



Figure 1.7: 16 inch Optical Telescope Assembly Prototype

The experimental work performed on this 16" OTAP will serve as guide for a future series of 1.4m(≈ 55 inches) Optical Telescope Assembly OTA with Adaptive Optics(AO) for the upgrade of the Navy Prototype Optical Interferometer(NPOI) in Flagstaff, Arizona, Figure 1.9. The upgrade will consists of changing the collecting optical surface from *Siderostats*² to telescopes. The prototype of the 1.4m, is a 16" which already is in its final completion stage as shown in Figure 1.8.

²A siderostat is a flat mirror which redirect the light from a star or object under observation.



Figure 1.8: OTAP on top of Adaptive Optics box



Figure 1.9: Aerial view of the Navy Prototype Optical Interferometer (NPOI)

CFRP materials are orthotropic, meaning that have at least 2 orthogonal planes of symmetry, where the material properties are independent of direction within each plane. This means that the properties of a single point in the telescope are different along each of the three mutually perpendicular axes, complicating the vibration

Chapter 1. Introduction

response studies. CFRP are the strongest and lightest material in use right now for telescope and optics construction. Some of the advantages of using it for telescopes and optics are

- Composite mirrors weight from 1/3 to 1/10 of mirror made using other technologies.
- CFRP materials exhibit low thermal expansion and being homogeneous, CFRP telescopes and optics do not suffer coefficient of expansion mismatch, thus simplifying telescope design.
- All-composite mirrors can be fabricated with aerial densities (mass per unit area) of between 0.7 kg per sq meter to 7.0 kg per sq meter.
- Composite mirrors are very rugged and unbreakable. They are vacuum stable as well as cryogenically stable and can be designed to exhibit a near zero coefficient of expansion.
- Composite mirrors can be fabricated from a wide range of composite materials allowing cost and design flexibility for a given application.

A big disadvantage of this new composite material telescope is the fact that this technology is under development; this is the first time a CFRP composite material telescope has been constructed of this size[10].

1.4.2 Vibration and flexure effects on imaging

Flexure and vibrations of the telescope mount translate into effects on the image. There are two main sources of vibrations: wind and motor drives³. When the wind

³This assumes that the telescope is controled remotely and that it is very well isolated from external ground vibrations.

Chapter 1. Introduction

pass through the telescope, the structure absorbs a surprising amount of energy, causing it to move about its center of gravity. When the wind calms or swirls, it will set up a vibration in the structure. There are three principal characteristics of mount vibrations,

- amplitude of oscillations
- frequency spectrum of oscillations
- damping time or relaxation time of the structure

Wooden and brass truss telescopes as with Galileo's and Newton's instruments typically have a frequency of several Hertz. The frequency can be increased by making the upper end lighter, by making the mirror box lighter, and by shorting the tube. Increasing the frequency is desirable as the overall dampening time will often shorten. Vibration caused by wind can be significantly reduced by removing as much as possible of the telescope cross section. Also for modern telescopes, the motor tracking system can induce vibration; any change from a completely smooth movement can induce vibration. A very important fact is, that if any of these frequencies coincide with the natural frequency of the telescope structure, the vibration would be not only induced but also amplified. Another consideration that needs to be taken into account is the deflection of the telescope structure due to gravity. This obviously misaligns the principal optical components, altering the image quality.

1.5 Introduction to Adaptive Optics and Adaptive Tip/Tilt corrector

As mentioned in section 1.3 atmospheric turbulence degrades the wavefront but there are techniques which help mitigate or correct for these effects. Babcock[11] was the

Chapter 1. Introduction

first to propose that by flattening the wavefront in the pupil of the imaging system this de-phasing could be corrected, also it was proposed independently to improve astronomical images but due to development cost this technique was not employed in astronomy until many years later. Defense research began using segmented mirrors to compensate for the effects of atmosphere in attempts to concentrate a laser beam on remote targets. Only in 1977 was the first adaptive optics system able to sharpen two-dimensional images and at the end of the 1970s systems were widely developed for defense applications. Through the success of the success of this technique in defense research, astronomers became interested in applications of this technique to astronomy[12].

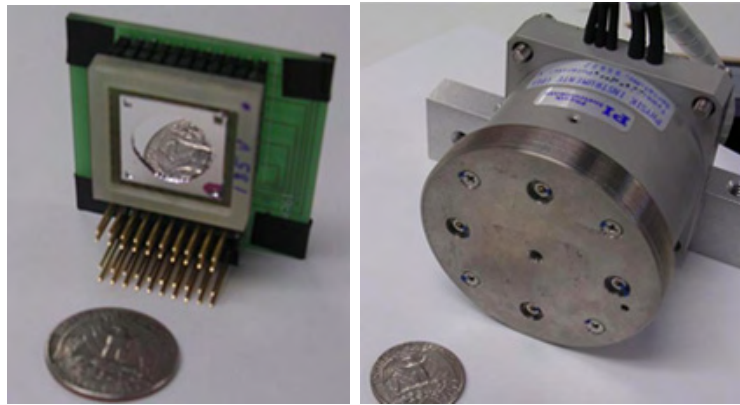
AO refers to optical systems which adapt to compensate for optical effects introduced by the medium between the object and its image. To perform this task, AO systems must perform two main functions:

- sense the wavefront deformation
- compensate in real-time for the deformation

A conventional adaptive optics system consists of three main subsystems, the wavefront sensor(WFS), an active or deformable mirror(DM) and a control computer. In a typical AO, the distorted light from the source enters the telescope and is first reflected from the DM. Some of the light is focused to form an image and some is diverted to the WFS, which measures the optical disturbance. The DM and WFS are connected to the main computer which takes measurements from the WFS and maps them into a real time control signal for the DM. The DM is a flexible mirror whose surface can be modified at high speeds by actuators at the back, Figure 1.10(a) shows the Micro-Electro-Mechanical 37 actuator DM from OKO Technologies used by the NRL group. If the described AO system works perfectly it should correct the primary(third order) aberrations. Nowadays, most conventional AO systems include

Chapter 1. Introduction

a fast steering mirror, usually mounted on a tip/tilt stage in order to minimize the amount of throw used by the DM in correcting global tilt, Figure 1.10(b). Sample of common AO system can be seen in Figure 1.11. In the AO system this fast steering mirror corrects for low order aberrations such as tip and tilt while the DM corrects for higher aberrations such as defocus, astigmatism, etc. The overall tip/tilt of the wavefront is responsible for the image jitter discussed in section 1.2. The Naval Research Laboratory(NRL) Wavefront Sensing & Control Division, moved a step forward by putting the DM on top of a tip/tilt stage reducing the number of reflections in an AO system, Figure 1.12(b) and 1.12(a). This is the first time, to the author's knowledge, that this has been done. This new technique arrangement, as seen in Figure 1.13, was the motivation behind the wavefront reconstructors algorithms which will be introduced and discussed in detail in further chapters. ⁴



(a) 37 actuator MEM, De- (b) Physik Instrumente S-340
formable mirror from OKO Fast Steering Mirror stage
Technologies

Figure 1.10: DM and stage

⁴For more information on this new technique refer to Christopher C. Wilcox's Master's thesis [13].

Chapter 1. Introduction

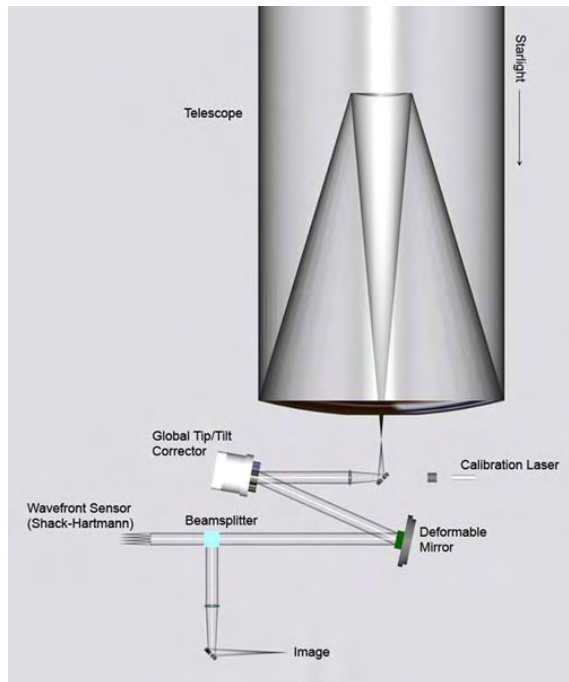


Figure 1.11: Sample setup of an AO system, Courtesy of C.C.Wilcox

Chapter 1. Introduction



(a)



(b)

Figure 1.12: Adaptive Tip/Tilt mirror:(a)AutoCAD drawing of the optical setup for the DM and Tip/tilt. (b)DM on Tip/tilt stage. Courtesy of C.C.Wilcox

Chapter 1. Introduction

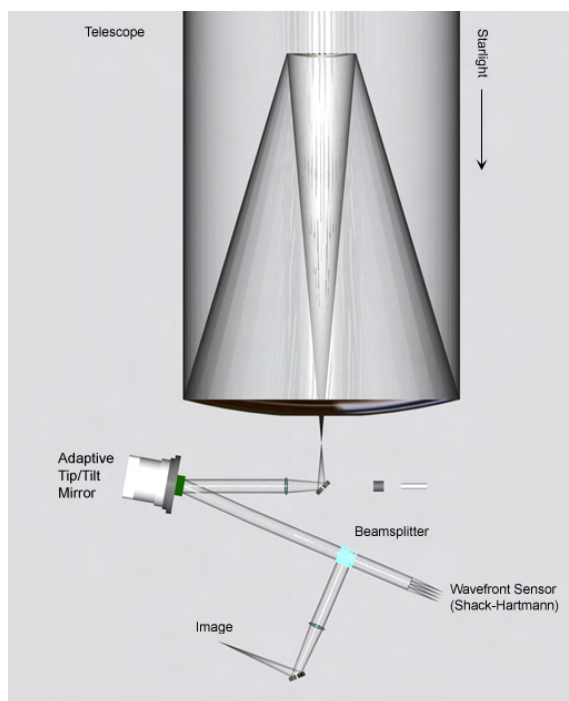


Figure 1.13: Sample setup of a new technique AO system, Courtesy of C.C.Wilcox

Chapter 1. Introduction

The Adaptive tip/tilt mirror shown in Figure 1.13(a) was used to gather data for the wavefront reconstructor. The main goals were to reconstruct the mirror surface and obtain an approximately global wavefront tilt induced by the stage. Such a study will demonstrate whether or not the DM surface, suffers any gross deflection while under movement.

1.5.1 Wavefront Sensor

The WFS is an instrument for optical testing of surfaces and optical metrology. There are two main types of WFS which at the same time, are divided in sub-categories[12][6]:

- direct in pupil plane: split the pupil into sub-apertures, and from the intensity deduce the wavefront phase
 - slope sensing
 - curvature sensing
- indirect in focal plane: the wavefront phase is deduced from the complete aperture intensity measurements
 - image sharpening
 - phase diversity

The main interest of this thesis is on a type of slope sensing wavefront sensor, the Shack-Hartmann WFS, due to its simplicity and availability for the experiments.

Shack-Hartmann WFS

The Shack-Hartmann WFS is a direct pupil plane sensor; it breaks up the wavefront in smaller sections which allowed the measurement of the propagation direction or tilt of each section of the wavefront. The more primitive Hartmann WFS consist of an array of apertures mounted at a distance from a 2-D recording device, Figure 1.14[14].

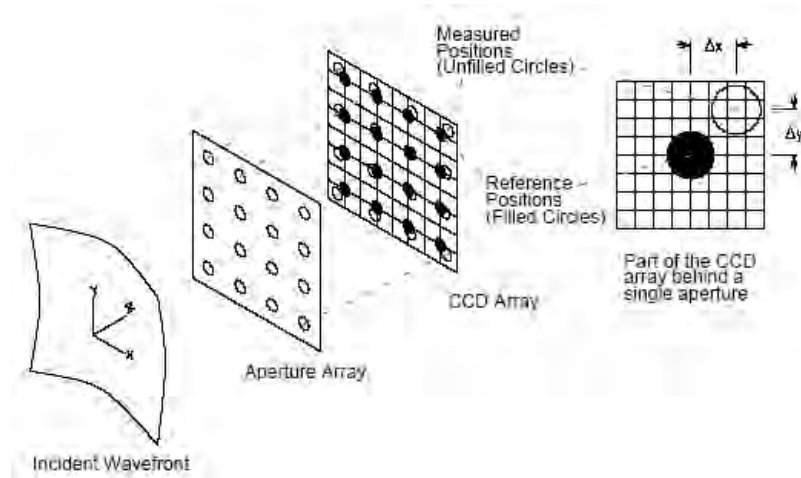


Figure 1.14: Drawing of a Hartmann Wavefront Sensor

Dr. Roland Shack around the 1960's replaced the Hartmann holes with lenses, so developing the Shack-Hartmann WFS (SHWFS). The SHWFS do not measure directly the wavefront phase, $\phi(x, y)$, instead it measures its spatial gradient (the Laplacian). Figure 1.15(a) shows a schematic of a SHWFS for an aberrated and plane wavefront.

Chapter 1. Introduction

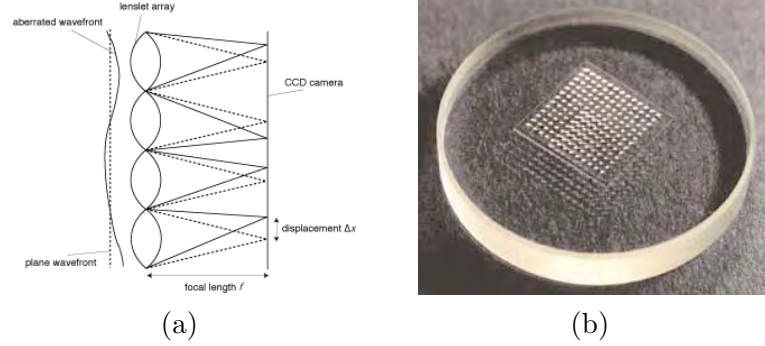


Figure 1.15: (a)Shack-Hartmann wavefront drawing. (b)Picture of lenslet array.

The SHWFS consist of a 2-D array of lenslet, Figure 1.15(b) that focus the wavefront into a 2-D measuring device, usually a Charge-couple device (CCD). The lenslet array used for taking data from the Adaptive Tip/Tilt mirror system was manufactured by Applied Optics Associates (AOA), Inc. If the incoming wavefront is plane and on axis, each lenslet forms an on axis image at the focus, which is used as a reference, Figure 1.16(a). If the wavefront is aberrated, each lenslet will form an image off-axis, Figure 1.16(b). This type sensor require a reference plane wave in order to calibrate the focus of the array. The SHWFS measures the tilt over each subaperture by comparing the position of the diffracted spot due to the reference plane wave and the position of the diffracted spot due to the aberrated wavefront. The position of the diffracted spot is calculated using a standard centroiding algorithm:

$$x = \frac{\sum_{i=i_{min}}^{i=i_{max}} \sum_{j=j_{min}}^{j=j_{max}} I(i, j) \cdot i}{\sum_{i=i_{min}}^{i=i_{max}} \sum_{j=j_{min}}^{j=j_{max}} I(i, j)} \quad (1.8)$$

$$y = \frac{\sum_{i=i_{min}}^{i=i_{max}} \sum_{j=j_{min}}^{j=j_{max}} I(i, j) \cdot j}{\sum_{i=i_{min}}^{i=i_{max}} \sum_{j=j_{min}}^{j=j_{max}} I(i, j)} \quad (1.9)$$

where $I(i, j)$ is the intensity by the pixel in the i th row and j th column[14]. The average gradient or slope of the wavefront can be calculated from the motion of the centroid of the diffracted spot produced by the aberrated wavefront, for example for

Chapter 1. Introduction

the x-axis

$$\frac{\partial \phi(x)}{\partial x} = \frac{\Delta x}{f} \quad (1.10)$$

where Δx is the difference between the position of the reference and aberrated spot position and f is the focal length of the SHWFS. From the obtained average gradients (the tilt information), an estimate of $\phi(x, y)$ is found from a phase reconstruction algorithm or wavefront reconstruction[6]. For more information on different wavefront

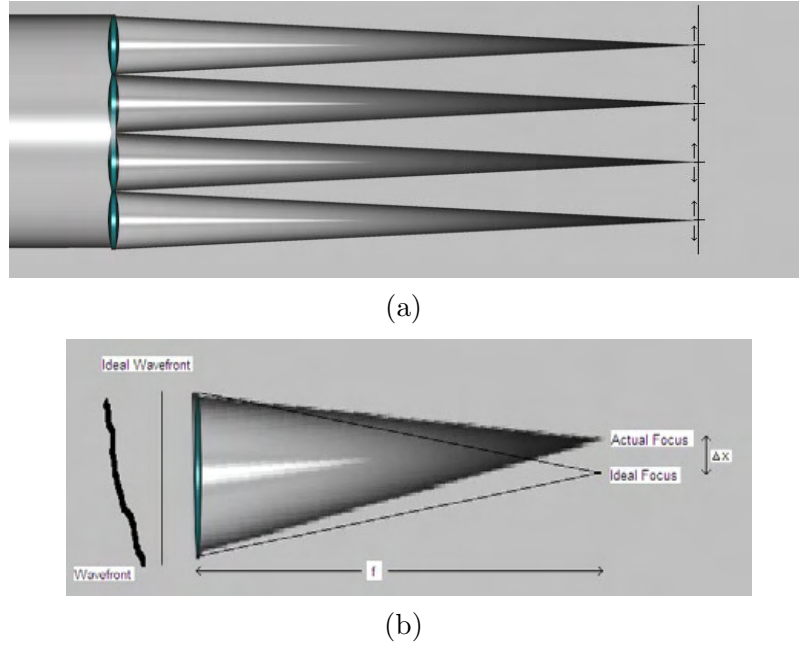


Figure 1.16: (a)SHWFS AutoCAD drawing, plane wavefront and, (b)aberrated wavefront focusing on the receiver's plane. Courtesy of C.C.Wilcox

sensors refer to J. Andrews master thesis[15].

Wavefront reconstructors

A WFS does not measure directly the phase, instead it measure the spatial gradient or the Laplacian of $\phi(x, y)$. The spatial gradient is referred as the wavefront slope

Chapter 1. Introduction

and the Laplacian as the curvature of it. What is measured by the SHWS is the spatial gradient of ϕ , given by

$$\nabla \vec{\phi} = \vec{\rho}(x, y) \tag{1.11}$$

This partial differential equation(PDE) can be solved using numerical methods.

Wavefront reconstruction is a laborious and time consuming inverse problem, from the measured data obtain an estimate of phase. The two main types of reconstructor algorithms are zonal and modal. In modal reconstruction the data is fit to a set of orthogonal surface polynomials (for example the Zernikes, [16]). Zonal reconstruction is a type of numerical integration where the phase is determined on a discrete set of points. There are many wavefront reconstructors algorithms that have been reported in literature[17][18][19]. This work focused on wavefront reconstructors firstly the Finite Difference method, similar to the one presented by Southwell in 1980 and modified by Zou in 2000. Secondly it will be discuss a finite element wavefront reconstructor as means of comparision. The first method was developed for square geometry lenslet arrays and the second was developed for non-square geometry.

Chapter 2

Wavefront Reconstruction (WFR)

2.1 Finite difference overview

Finite difference method(FDM) is a classical way of numerically solving PDEs. The FDM consist of transforming a continuous domain to a mesh of discrete points, converting the PDE into a set of equations which can be solved. The FDM can be implicit, meaning that the PDE can be solved by solving a system of simultaneous linear equations and convergence is always assured, or explicit meaning that the PDE can be solved using the appropriated boundary conditions and convergence is assured for specific sizes of increment interval lengths. There are three approximations that can be made to evaluate the value of the first partial derivative of the given PDE, the central, forward and backward difference scheme[20].

Recall that the SHWFS provides a discretization of the incoming wavefront onto a set of equally spaced grid points. As already stated in the last chapter, this means that the SHWFS measures the gradient of the phase of the incident light,

$$\nabla \vec{\phi} = \vec{\rho}(x, y) \tag{2.1}$$

Chapter 2. Wavefront Reconstruction (WFR)

In other words what is obtained is a grid of points for which we want to approximate the solution of the PDE given by equation 2.1. Due to the geometry of the grid (SHWFS lenslet array), the central difference scheme was chosen to approximate the phase at the grid points, which is conceptually shown in Figure 2.1. Considering only the x measurements, take the slopes at point 1 and point 2, perform an average obtaining a new point by application of the following formula

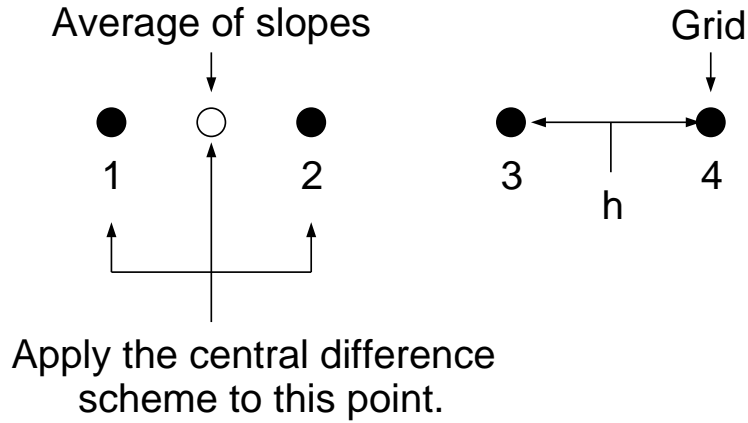


Figure 2.1: Application of the central difference scheme

$$\frac{S_2^x + S_1^x}{2} = \frac{\phi_2 - \phi_1}{h} \quad (2.2)$$

where S^x is slope measurement at the specific point, ϕ is the phase at the grid point and h is the separation between grid points. Generalizing the scheme for x and y slope measurements we obtain:

$$\frac{S_{i+1,j}^x + S_{i,j}^x}{2} = \frac{\phi_{i+1,j} - \phi_{i,j}}{h} \quad \begin{matrix} i=1, N-1 \\ j=1, N \end{matrix} \quad (2.3)$$

$$\frac{S_{i,j+1}^y + S_{i,j}^y}{2} = \frac{\phi_{i,j+1} - \phi_{i,j}}{h} \quad \begin{matrix} i=1, N \\ j=1, N-1 \end{matrix} \quad (2.4)$$

where N is the number of phase points in one of the direction. For our grid example $N = 4$. Now note that equations 2.3 and 2.4 can be written in a single matrix

Chapter 2. Wavefront Reconstruction (WFR)

equation of the form:

$$\mathbf{D}\mathbf{S} = \mathbf{A}\phi \quad (2.5)$$

where \mathbf{D} is a sparse matrix containing the average of the slope, \mathbf{S} is a vector containing the slope measurements, x data first, \mathbf{A} is a sparse matrix containing the phase difference values and ϕ is a vector of the unknown phase values. An important thing in the construction of the linear system is the way the \mathbf{S} and ϕ vectors are stored. The general sparse matrix and the structure is shown in Figure 2.2

$$\begin{array}{c} \mathbf{A} \\ \left[\begin{array}{c} \textcircled{1} \\ N(N-1) \times N^2 \\ \hline \textcircled{2} \\ N(N-1) \times N^2 \end{array} \right] \end{array} \begin{array}{c} \mathbf{f} \\ \left[\begin{array}{c} \textcircled{3} \\ N^2 \\ \times \\ 1 \end{array} \right] \end{array} = \begin{array}{c} \mathbf{D} \\ \left[\begin{array}{c} \textcircled{4} \\ N(N-1) \times 2N^2 \\ \hline \textcircled{5} \\ N(N-1) \times 2N^2 \end{array} \right] \end{array} \begin{array}{c} \mathbf{S} \\ \left[\begin{array}{c} \textcircled{6} \\ 2N^2 \\ \times \\ 1 \\ \textcircled{7} \end{array} \right] \end{array}$$

Figure 2.2: General dimensions for a FD N X N matrix formation

2.2 Results for FD

This section presents the results for the FD reconstructor. More results will be presented in Chapter 3. The Adaptive Tip/Tilt mirror stage, Figure 2.3, was driven at 30 Hz and 90° out of phase by software developed by Narrascope Inc, resulting in a circular motion of the spots at the SHWFS, representing global Tip/Tilt. Data was taken for three different configurations of the tip/tilt stage mirror system. The configurations were as follow:

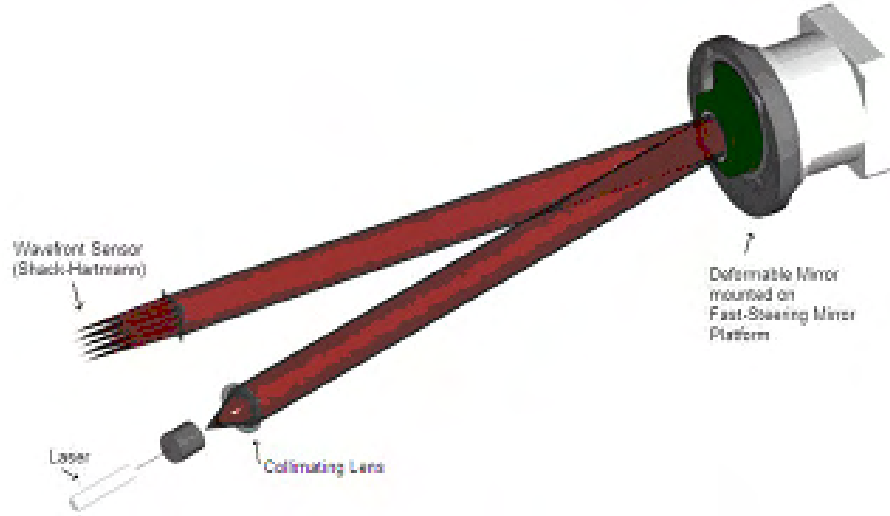


Figure 2.3: Adaptive Tip/Tilt: Drawing of the system under study. Courtesy of C. Wilcox

- **Configuration 1:** A flat mirror was placed on the tip/tilt stage, a reference frame was captured with the stage off, multiple frames with the stage on.
- **Configuration 2:** The OKO DM unpowered was placed on the tip/tilt stage, a reference frame was captured with the stage off, multiple frames with the stage on.
- **Configuration 3:** The OKO DM powered was placed on the tip/tilt stage, a reference frame was captured with the stage off, multiple frames with the stage on.

The three configurations underwent the same procedure, with the difference being the change of mirrors on the tip/tilt stage.

An image obtained from the Adaptive Tip/Tilt mirror and SHWFS system is shown in Figure 2.4. Also it shows the points where the solution was approximated and the reconstructed wavefront for a single frame.

Chapter 2. Wavefront Reconstruction (WFR)

The results obtained by reconstructing the wavefront by FD are shown in Figures 2.5-2.7 with the axis been arbitrary matlab units. Figure 2.5 shows the reference frame used, and the reconstructed wavefront for three other frames. The same is shown in the other graphs but for the OKO DM unpowered and powered. Frames (a)-(c) where taken at different times, meaning tip/tilt stage moved by an unknown angle but constant with respect to the z axis, if the stage produced a constant repeatable movement. For each of the frames (a) its contour was plotted. Qualitatively it can be said that the contour for the flat mirror showed that the lines where all approximately equidistant over the complete surface, but in one of the corners it appears certain structure. This structure is from the mirror itself, what it was to be flat was not flat. This may be due to the thickness or deformation on the surface of it. The results from the DM does not show any big deformation, meaning that it was flatter in both cases, unpowered and powered. Also, the contour of the OKO unpowered the lines are more equidistant than for the OKO powered and this can be a sign of stress on the surface.

Chapter 2. Wavefront Reconstruction (WFR)

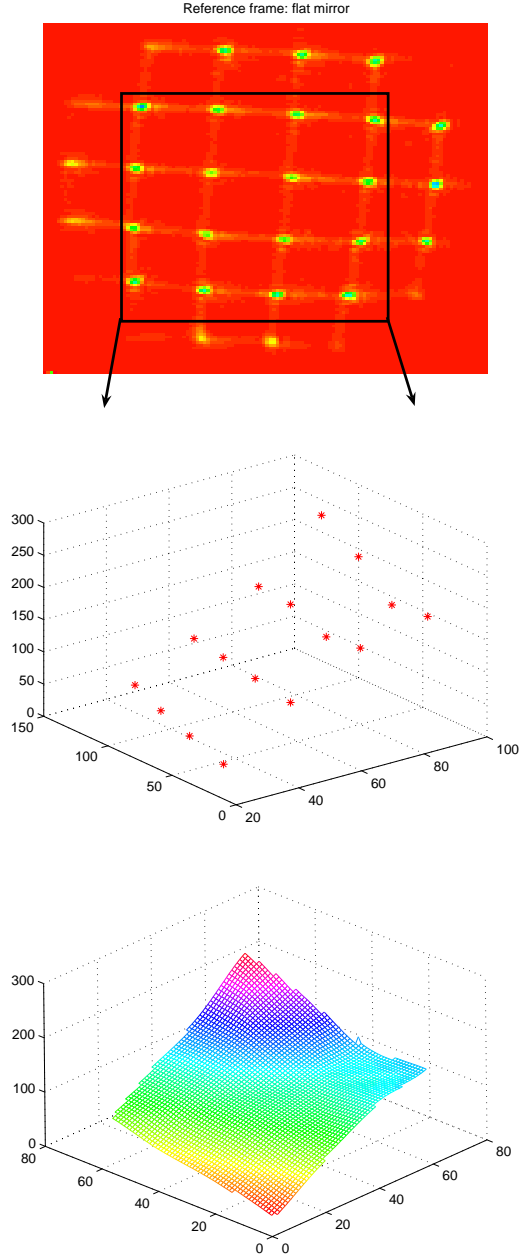


Figure 2.4: FD:(Top:)Shows the reference frame for the flat mirror. The square show the selected spots for the reconstruction. (Middle:)Each star represent the approximate solution for the phase at the selected spots. (Bottom:)Reconstructed wavefront

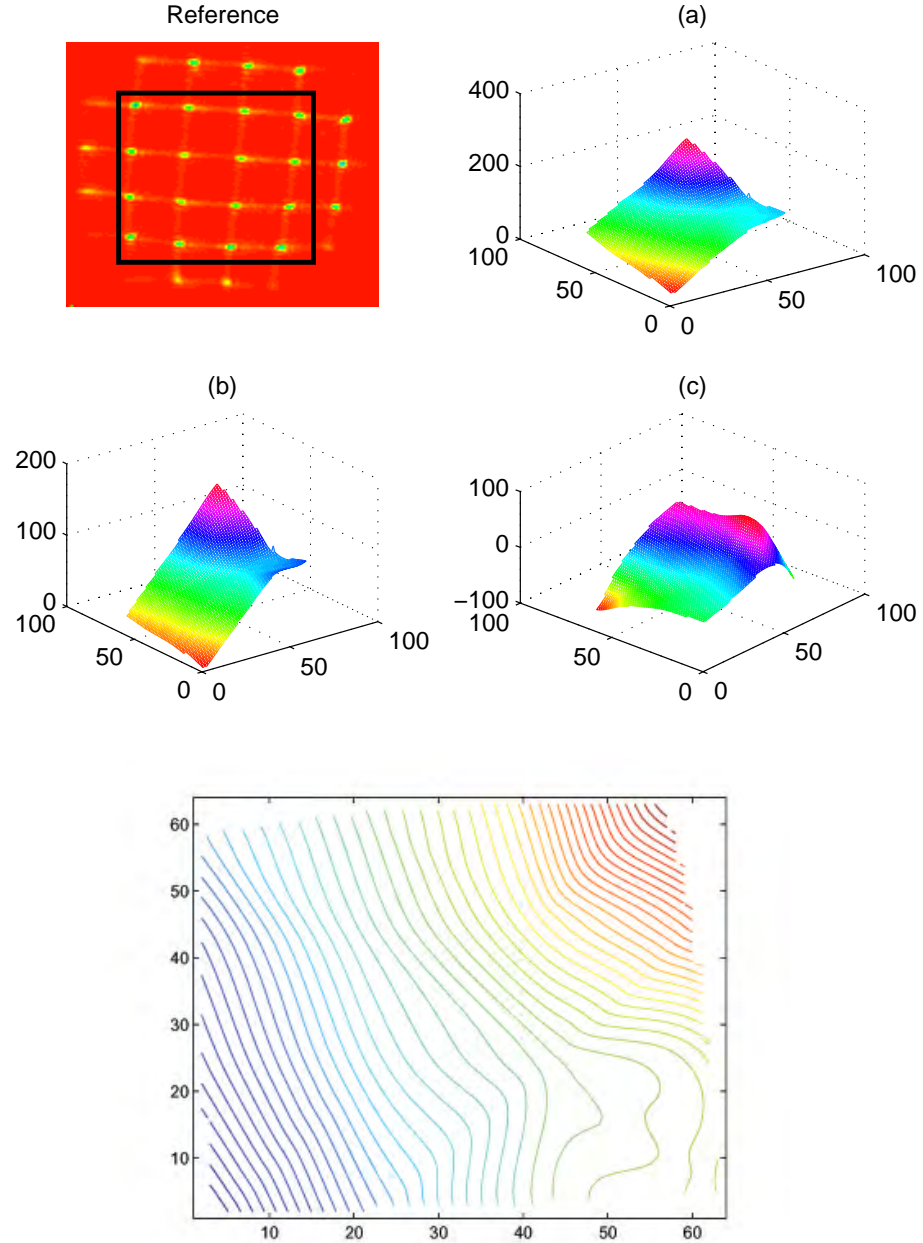


Figure 2.5: FD:(Top-Right:)Reference frame for the flat mirror and square with the selected spots.(a)Reconstruction for flat frame1. (b)Reconstruction for flat frame2. (c)Reconstruction for flat frame2.(Bottom:)Contour of flat frame1, showing deformation on the lower-right corner.

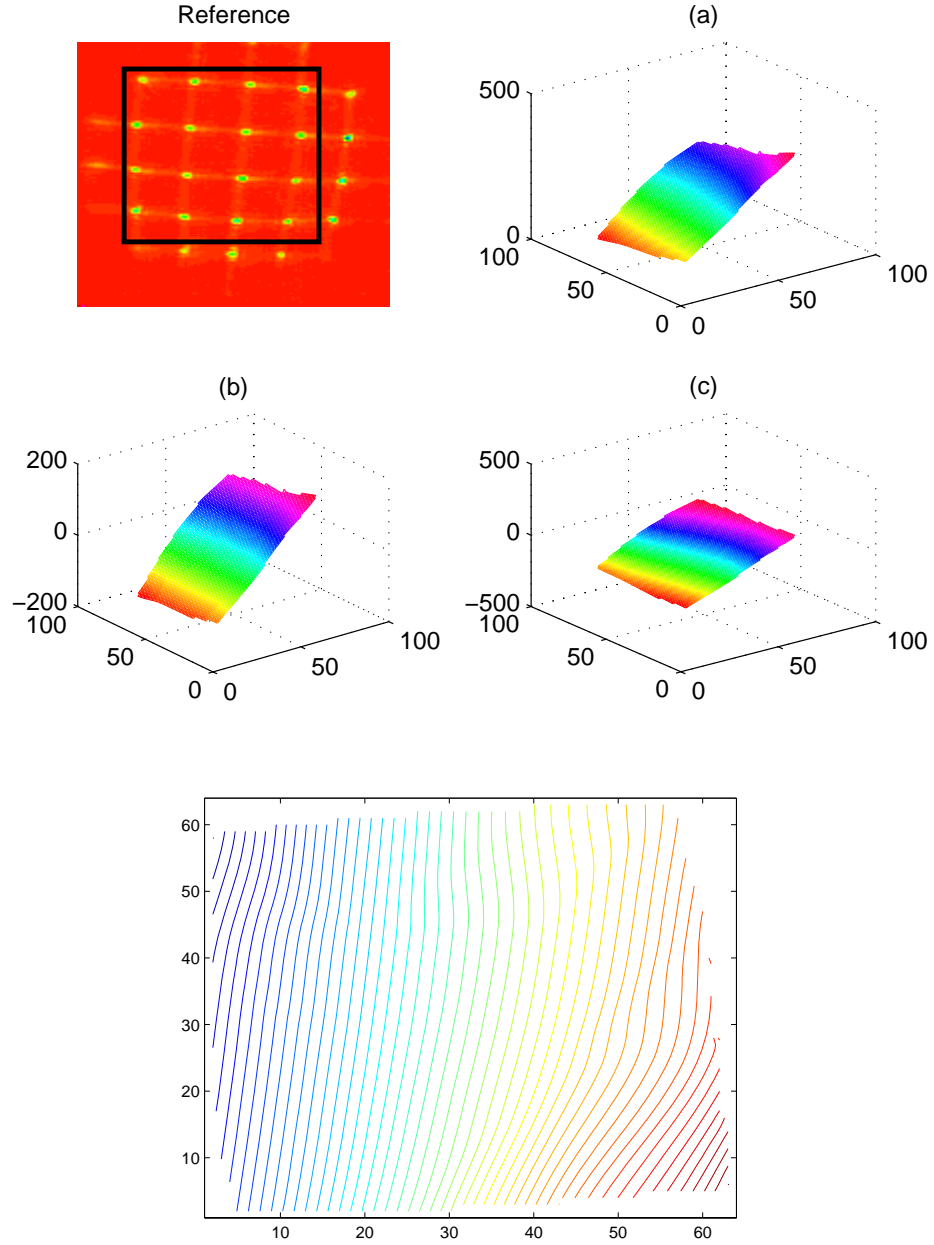


Figure 2.6: FD:(Top-Right:)Reference frame for the OKOunp mirror and square with the selected spots.(a)Reconstruction for OKOunp frame1. (b)Reconstruction for OKOunp frame2. (c)Reconstruction for OKOunp frame2.(Bottom:)Contour of OKOunp frame1, showing to be flatter than the flat.

Chapter 2. Wavefront Reconstruction (WFR)

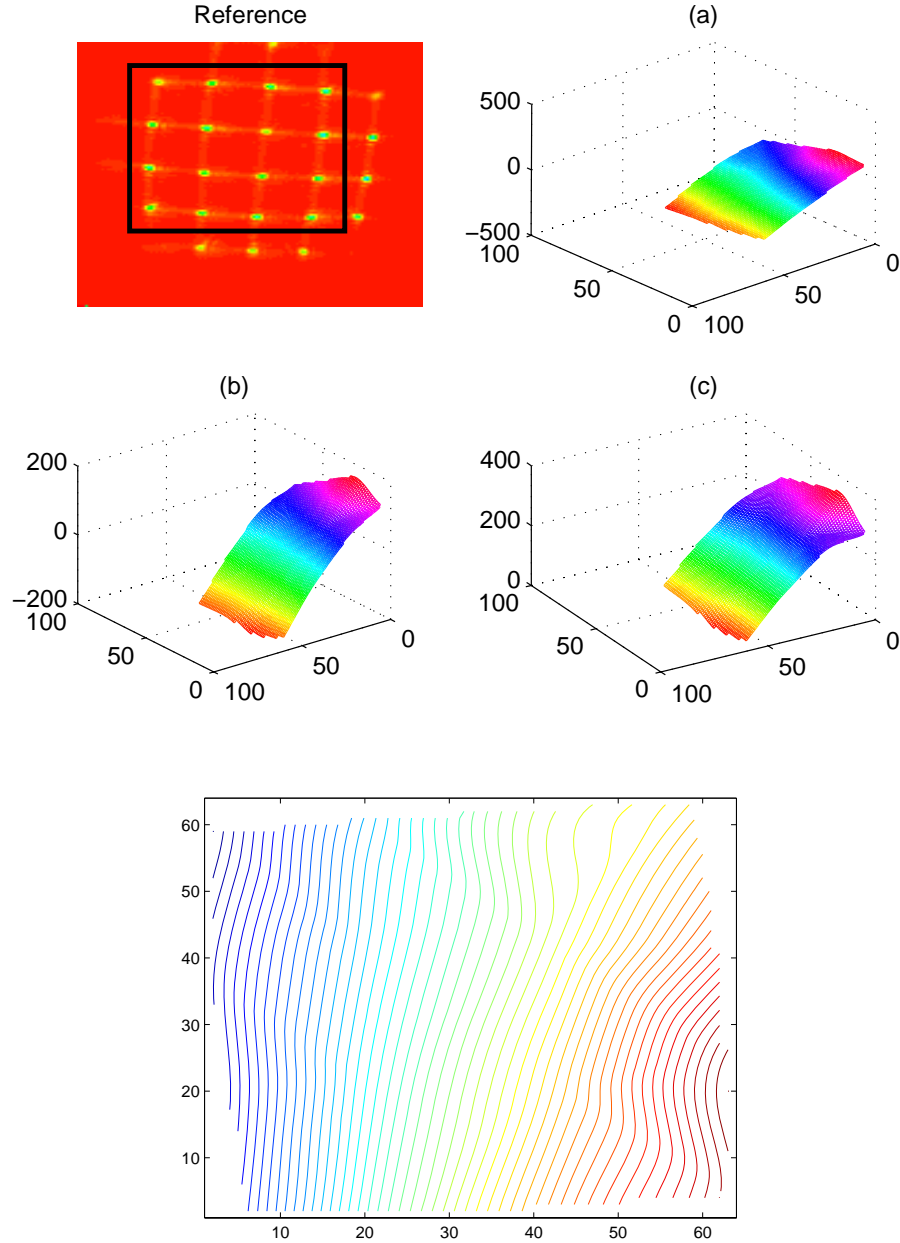


Figure 2.7: FD:(Top-Right:)Reference frame for the OKOp mirror and square with the selected spots.(a)Reconstruction for OKOp frame1. (b)Reconstruction for OKOp frame2. (c)Reconstruction for OKOp frame2.(Bottom:)Contour of OKOp frame1, showing to be flatter than the flat.

2.3 Finite element overview

The Finite Element Method(FEM) is a numerical technique for solving problems which are described by ordinary or partial differential equations. A continuous physical problem is transformed into a discretized finite element problem. As in the Finite Difference Method (FDM) a problem is formulated which is described most commonly by a partial differential equation and an approximate solution is found by using FEM. For the SHWFS used, what is measured can be express by the differential equation given by

$$\vec{\nabla}\Phi(x, y) = \vec{\rho}(x, y) \quad (2.6)$$

The SHWFS measurements define the vector, $\vec{\rho}(x, y)$ and what is wanted is Φ . If the divergence of equation 2.6 is taken resulting in

$$\nabla^2\Phi(x, y) = \vec{\nabla} \cdot \vec{\rho} \quad (2.7)$$

it is obtained the Poisson's equation for which the solution by finite element methods is well studied [21],[22][23]. Noll suggested that solutions to the wavefront reconstruction problem are similar to solutions of the Poisson's equation with Neumann boundary conditions [24].

FEM discretize the domain of a function in what is call *elements* which are defined by *nodes*. There are two types of *nodes*, the *global nodes* which are the points in the domain where the function values is know and the *elements nodes* which are the nodes that define the geometry of the element, Figure 2.8.

Chapter 2. Wavefront Reconstruction (WFR)

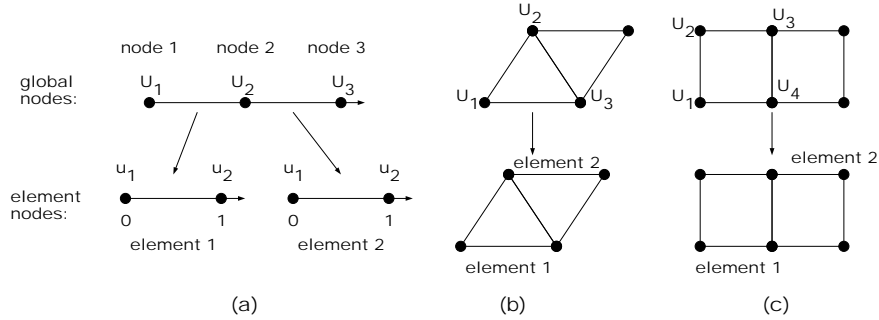


Figure 2.8: (a) Identifying the difference between *element nodes* and *global nodes*. (b-c) Different elements configuration

The wavefront reconstructor based on FEM was developed for the use in the Horizontal path propagation measurements over the sea, HOPA[25, 26, 27]. The HOPA experiment consisted on measuring the turbulence strength parameter, C_n^2 , over the water[28, 29]. The hardware of the HOPA experiment contained a SHWFS arrangement similar to the one used on the Adaptive Tip/Tilt mirror system. The main difference of this two experiments was the geometry of the lenslet array used, as mentioned before the Adaptive Tip/Tilt used a square grid of lenslet and the HOPA used non-square arrangement where the lenslets are shifted, as shown in Figure 2.9.

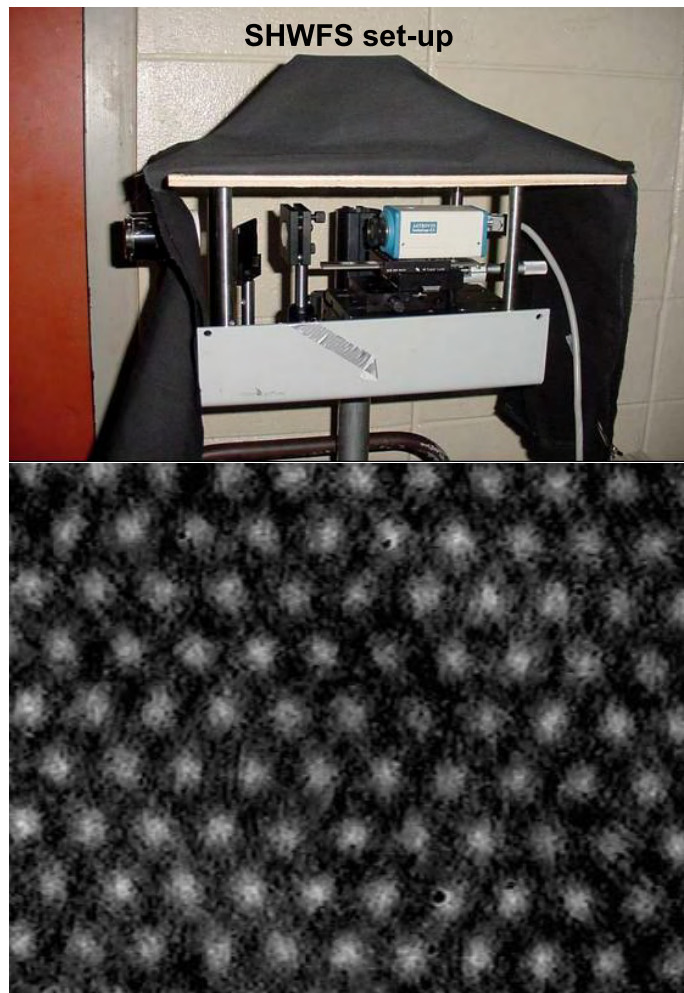


Figure 2.9: (Top:)HOPA experiment SHWFS optical set-up. (Bottom:)Spots from the SHWFS.

Since the geometry allowed, the FEM WFR used in HOPA was implemented also on the Adaptive Tip/Tilt system with the idea of corroborating the results obtained from the FD WFR. The solution to both method should be the same, this way proving if the FD was implemented correctly.

2.4 Results FE

Figure 2.10 shows the reference frame used, and the reconstructed wavefront for three other frames. The exact same procedure and data frames as in the FD wavefront reconstructor were used for this part. Qualitatively it can be said that the results are the same and clearly the contour for the flat mirror showed the same structure at one of the corners, shown inside the circle. Also the same results as before can be seen in the contour plot for the other two configurations.

The results obtained by reconstructing the wavefront by FE are shown in Figures 2.11-2.13 with the axis been arbitrary matlab units.

It is interesting to note that the reconstructed wavefronts for the unpowered and powered states are very similar, showing that there is minimal distortion caused by the membrane being powered and unpowered. Also, this result demonstrated that the distortion of the DM surface is minimal when it is being moved physically on the tip/tilt platform.

Chapter 2. Wavefront Reconstruction (WFR)

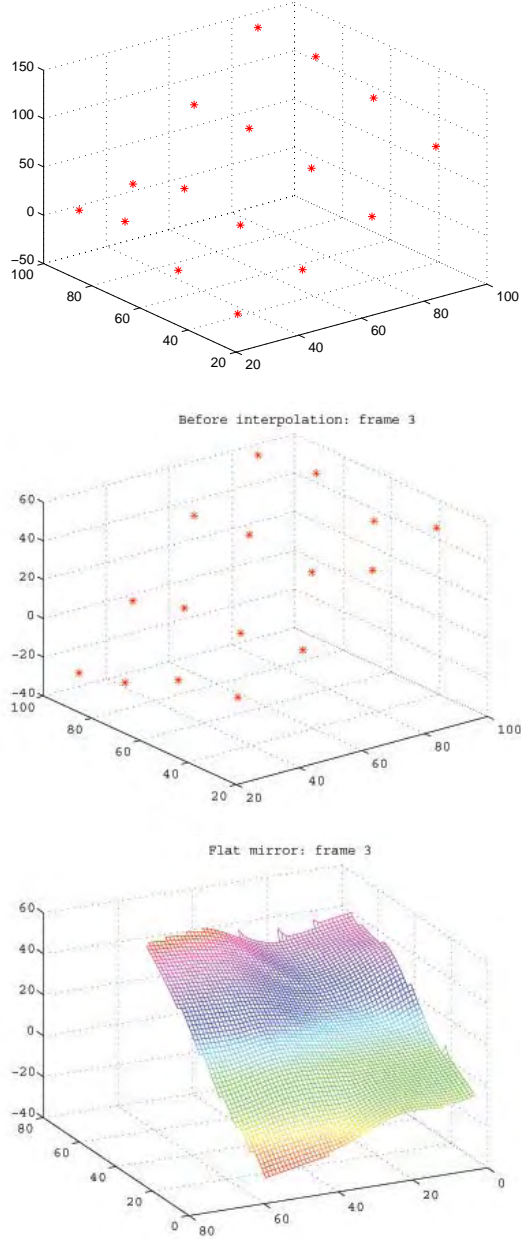


Figure 2.10: FE:(Top:)Shows the reference frame for the flat mirror. The square show the selected spots for the reconstruction. (Middle:)Each star represent the approximate solution for the phase at the selected spots. (Bottom:)Reconstructed wavefront

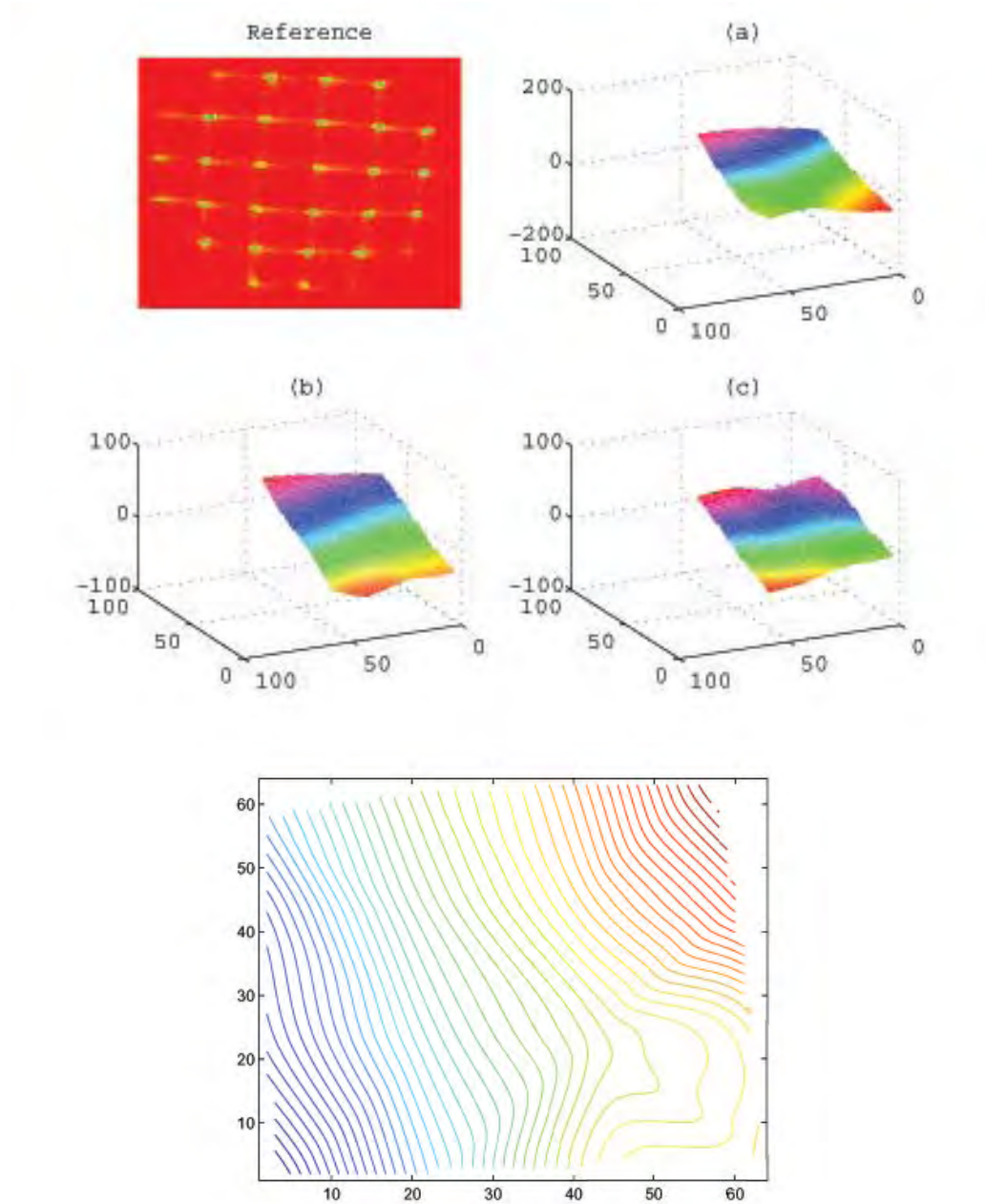


Figure 2.11: FE:(Top-Right:)Reference frame for the flat mirror and square with the selected spots.(a)Reconstruction for flat frame1. (b)Reconstruction for flat frame2. (c)Reconstruction for flat frame2.(Bottom:)Contour of flat frame1, showing deformation on the lower-right corner as in FD.

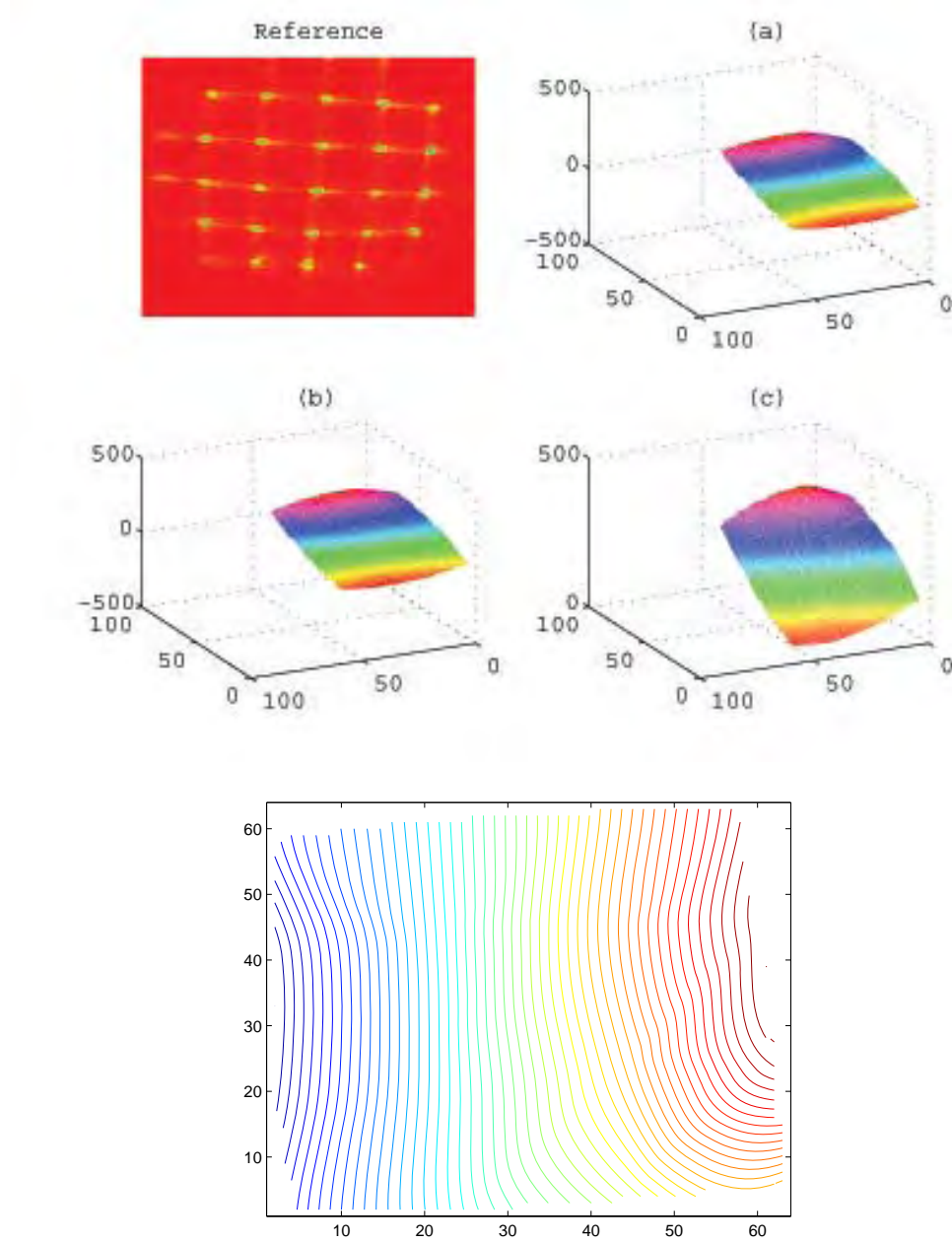


Figure 2.12: FE:(Top-Right:)Reference frame for the OKOunp mirror and square with the selected spots.(a)Reconstruction for OKOunp frame1. (b)Reconstruction for OKOunp frame2. (c)Reconstruction for OKOunp frame2.(Bottom:)Contour of OKOunp frame1, showing to be flatter than the flat.

Chapter 2. Wavefront Reconstruction (WFR)

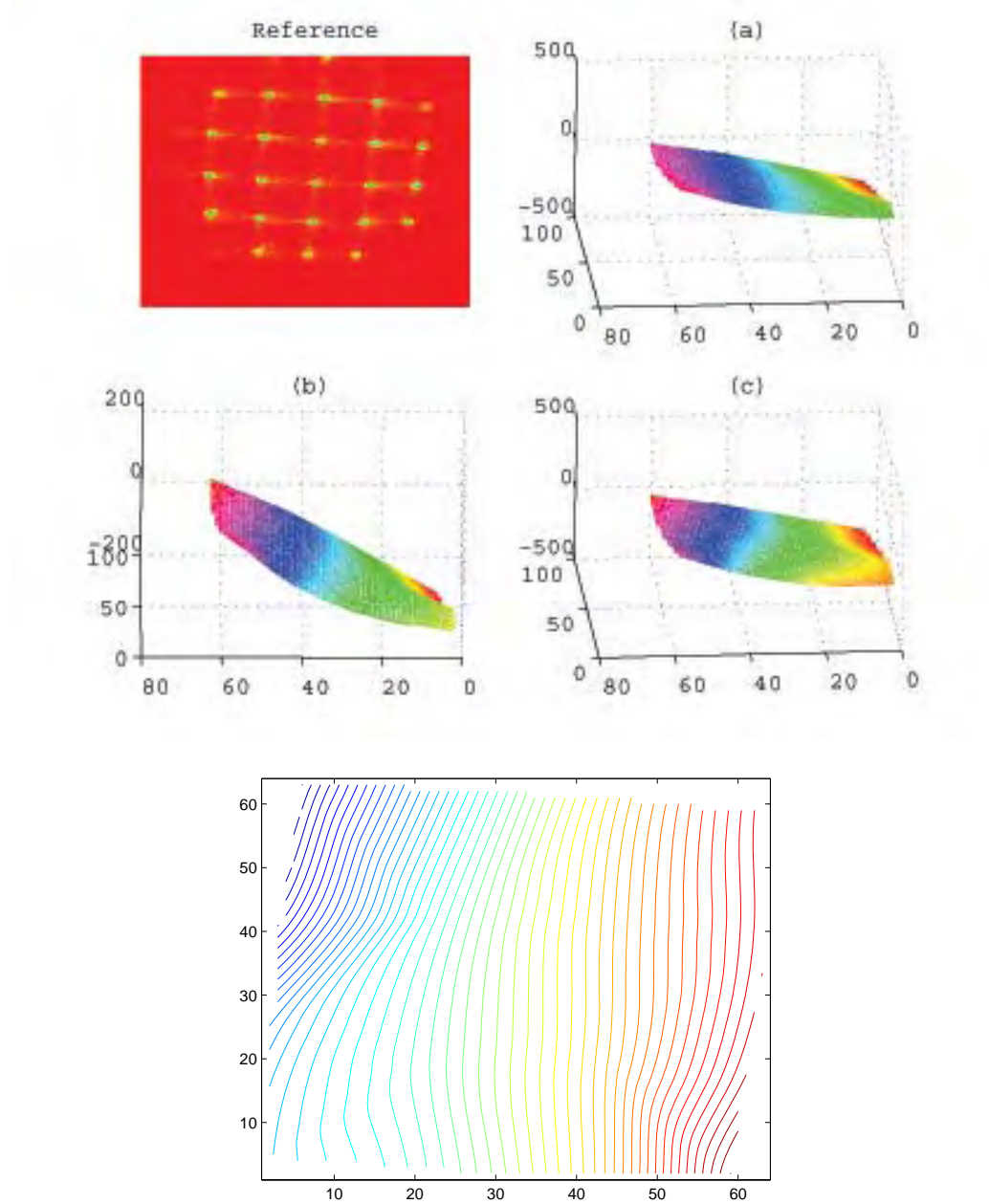


Figure 2.13: FE:(Top-Right:)Reference frame for the OKOp mirror and square with the selected spots.(a)Reconstruction for OKOp frame1. (b)Reconstruction for OKOp frame2. (c)Reconstruction for OKOp frame2.(Bottom:)Contour of OKOp frame1, showing to be flatter than the flat.

Chapter 3

Comparison between FD and FE

Theoretically, with the FD and FE working properly and in an aberration-free system, the mirror's surface can be extrapolated from this data, being this the main intention of the application of these two methods. Unfortunately, aberrations from other optics, programming errors, wrong selection of boundary conditions for the methods made this difficult to accomplish. Chapter 2 showed the approximate reconstructed surface for the flat mirror and for the DM in its two different configurations. The reconstructor code process for both methods can be seen in the flowchart in figure 3.1. A general GUI was created in Matlab, with instruction boxes, in order to manage the input of parameters and as a guide for first time users, Figure 3.2. Also an important part of the code is the reference parameters. These parameters are obtained from the reference wavefront frame. Figure 3.3 shows the GUI for selecting the mask which will be used throughout the code. The user select a submask of certain size, this way reducing the "bleeding" between the spots and minimizing the area for calculating the centroid position of each of the focused spots inside each.

An important results obtained from both reconstructor was the large amount of

Chapter 3. Comparison between FD and FE

tilt found in all of these reconstructed wavefronts, as expected due to the steering platform inducing it. Once the wavefronts for different configurations were reconstructed using the two reconstruction methods, in order to obtain a global tilt estimate, planes were fit to the overall wavefront. This was done by selecting 3 points on the wavefront and solving for the normal to the plane they created, as shown in Figure 3.4. Normals were calculated for various points around the surface of the wavefront and plotted at the origin of a coordinate system, as shown in figure 3.5. These normals, for each case, were then averaged together as shown in figure 3.5 by the red and dashed line. This procedure was performed for the three configurations. The normals were quite similar showing that the global tilt was generally the same for each wavefront measurement to an error of $\pm 0.08 \text{ units}$.

Table 3.1 shows the approximate angle, in degrees, of the reconstructed wavefronts from the reference, for which the reason for the number of decimal points is only due to Matlab. This similarity in the angles shows that the Tip/Tilt stage was working in a repeatable manner, due to the fact that the angle seems to almost maintain constant. An average percent difference of the normals for each method is shown in Table 3.2. Also, the execution time for solving the linear system of equations by Gaussian Elimination, was obtained from the use of the Matlab commands *tic* & *toc*, is shown in Table 3.3.

Both reconstruction methods results are very similar. For example, considering the table for the calculated angles and comparing the results for the three configurations it is clear the similarity between the two DM states and the small difference between those results from the flat mirror. A reasonable explanation for the difference in these results, is the fact of misalignment at the time of taking out the flat mirror from the stage and placing the DM on it. For the FD method and approximate error between the flat and the DM tilt is on the order of $\pm 0.14 \text{ units}$ and for the FE method in the order of $\pm 0.12 \text{ units}$, proving the similarity in the results for both

Chapter 3. Comparison between FD and FE

Table 3.1: Approximate calculation of tip and tilt

Tip and Tilt angle, θ_i , ± 0.1 degrees						
Method	Type of mirror	θ_1	θ_2	θ_3	θ_{mean}	$std(\theta_{123})$
FD	Flat	60.4	65.9	66.1	64.1	3.23
	OKO Unpowered	52.2	51.9	51.5	51.9	0.35
	OKO Powered	51.9	51.4	51.5	51.6	0.26
FE	Flat	58.3	61.6	67.0	62.3	4.39
	OKO Unpowered	52.3	52.0	51.8	52.0	0.25
	OKO Powered	51.0	50.5	50.7	50.7	0.25

Table 3.2: Percent Difference for the Tilt, θ_{mean} , calculation between the two methods

Percent Difference θ_{mean} , ± 0.1 units		
Method	Type of mirror	Percent Difference %
FD \Leftrightarrow FE	Flat	2.9 %
	OKO Unpowered	3.5 %
	OKO Powered	1.7 %

methods. This results showed that the FD reconstructor works and also that the FE reconstructor could be used for both experiments, the Adaptive Tip/Tilt and HOPA due to its flexibility in the geometry.

Table 3.3: Execution time for the solution of the linear system

Execution time, t in seconds, ± 0.001 seconds	
Method	GE
FD	0.0780
FE	0.0010

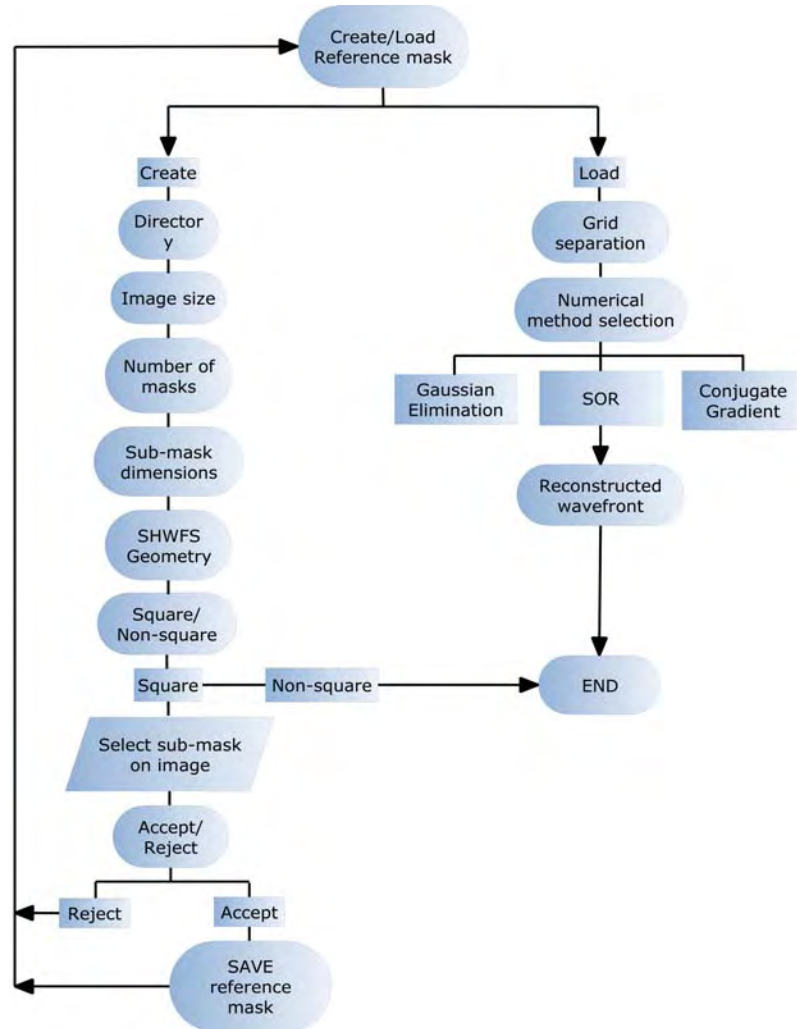


Figure 3.1: Flowchart for both of codes methods, FD and FE

Chapter 3. Comparison between FD and FE

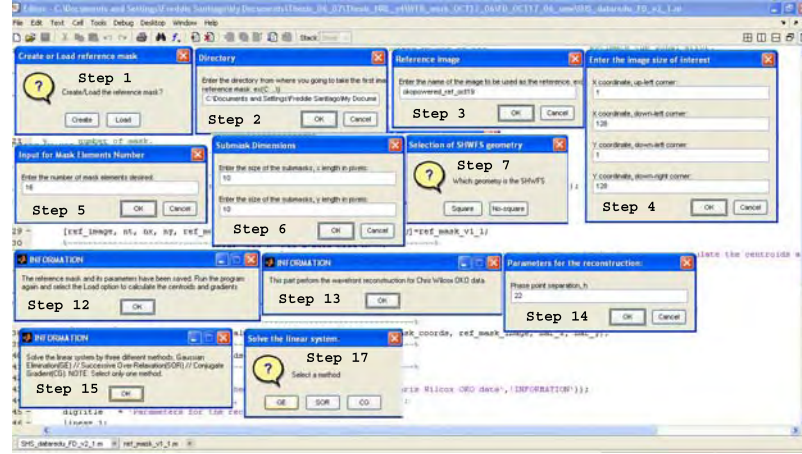


Figure 3.2: GUI created in Matlab for the codes

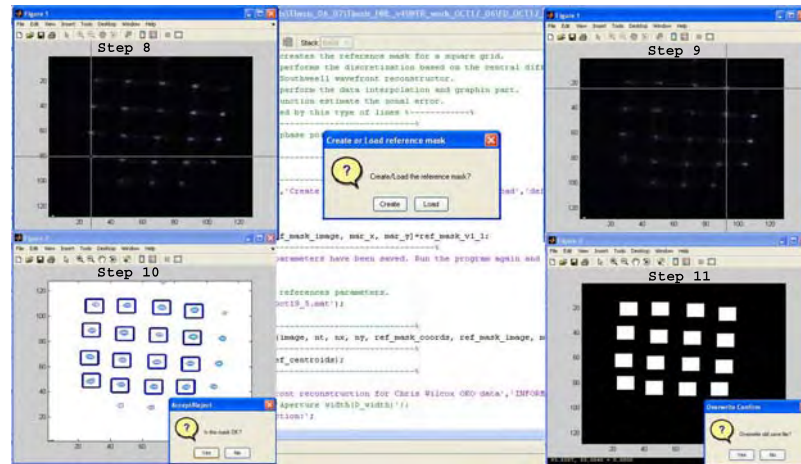
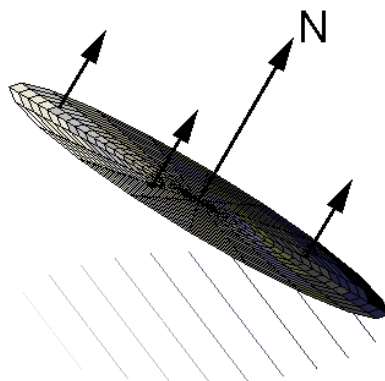
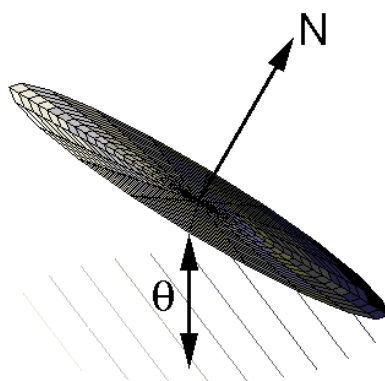


Figure 3.3: Selection of the mask from the reference image



(a) Tilt plane, its normals and average



(b) Tilt angle θ

Figure 3.4: Planes normals and average

Chapter 3. Comparison between FD and FE

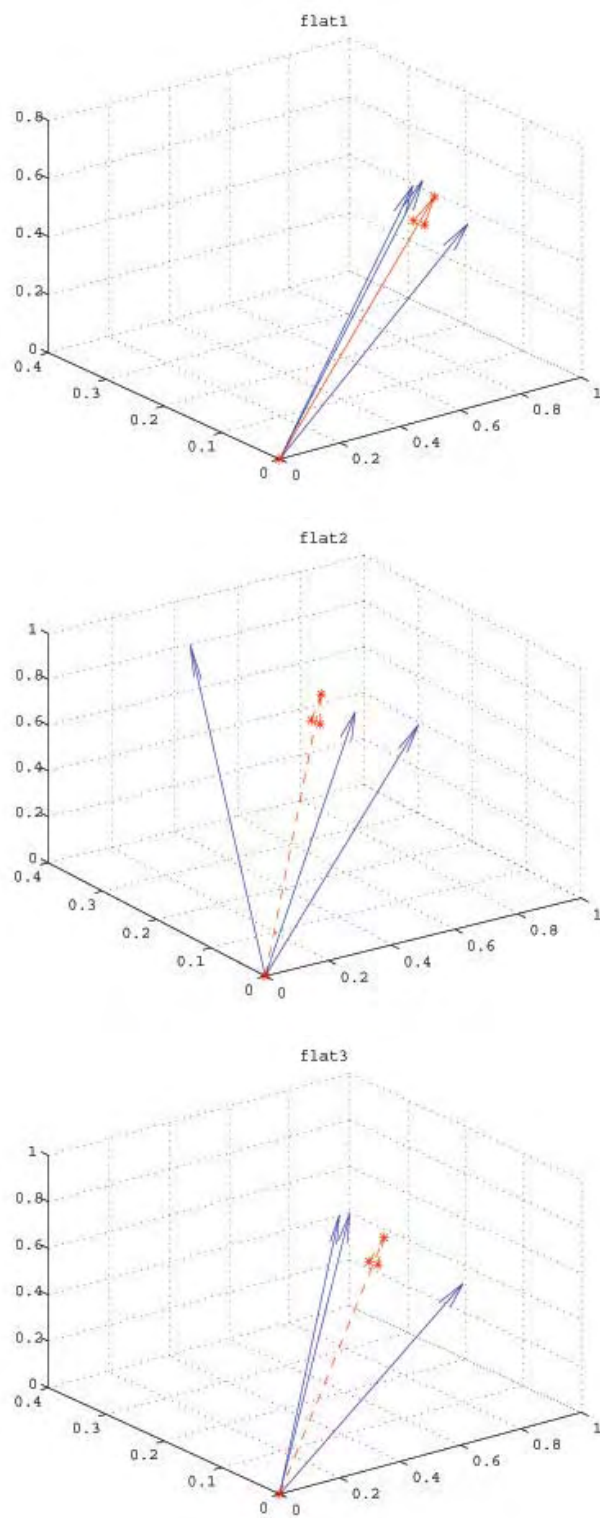


Figure 3.5: Normals for flat1 and their respective average in dashed line, FD

Chapter 3. Comparison between FD and FE

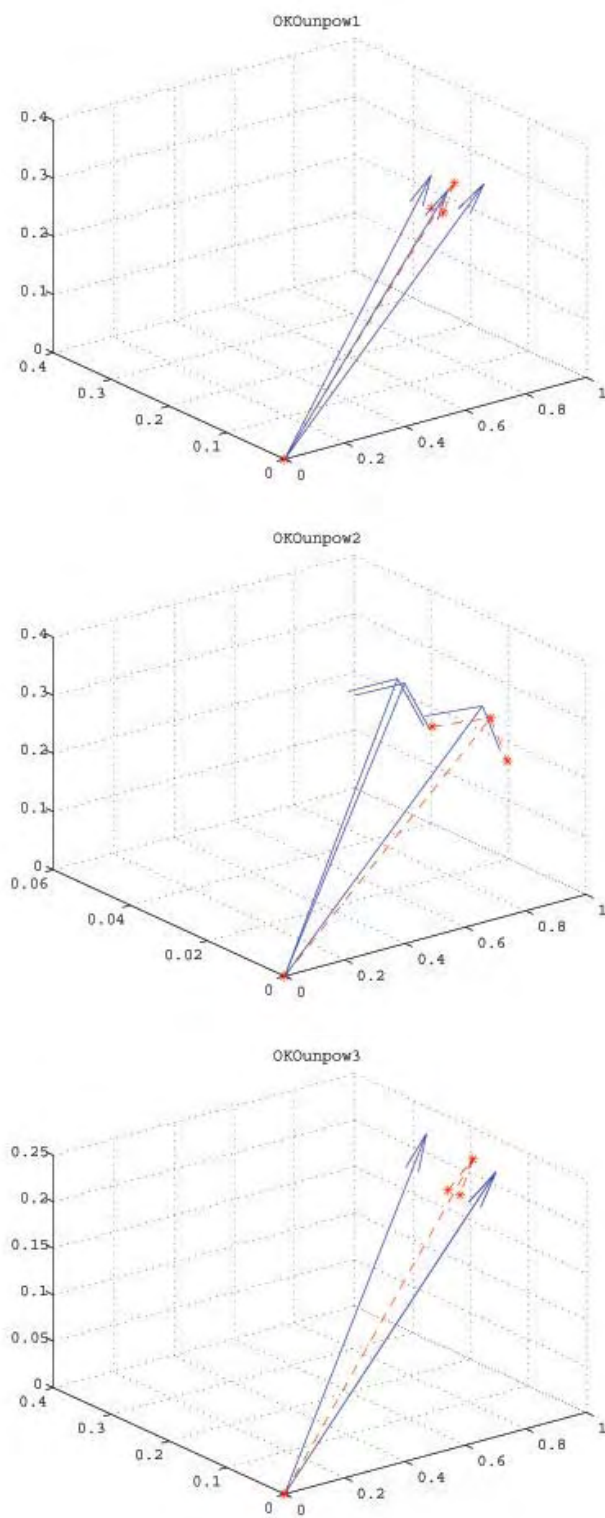


Figure 3.6: Normals for OKOunpow and their respective average in dashed line, FD

Chapter 3. Comparison between FD and FE

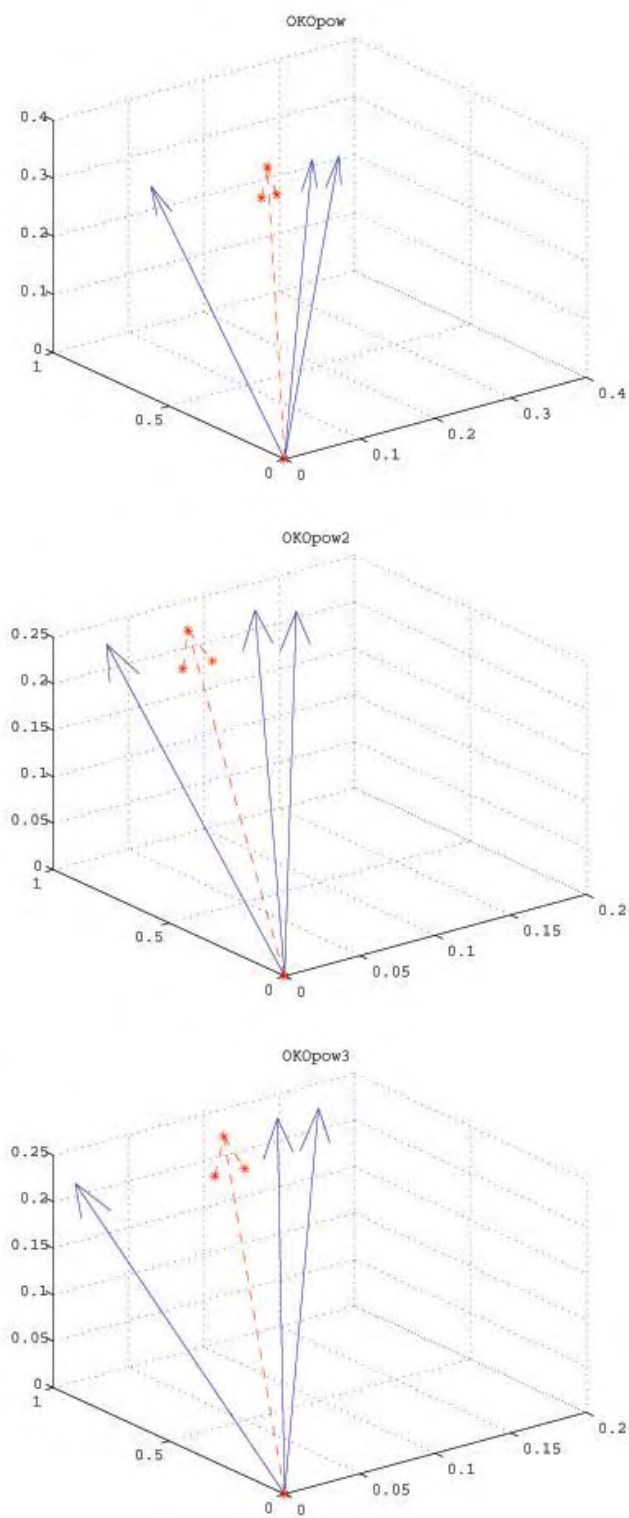


Figure 3.7: Normals for OKOpow and their respective average in dashed line, FD

Chapter 3. Comparison between FD and FE

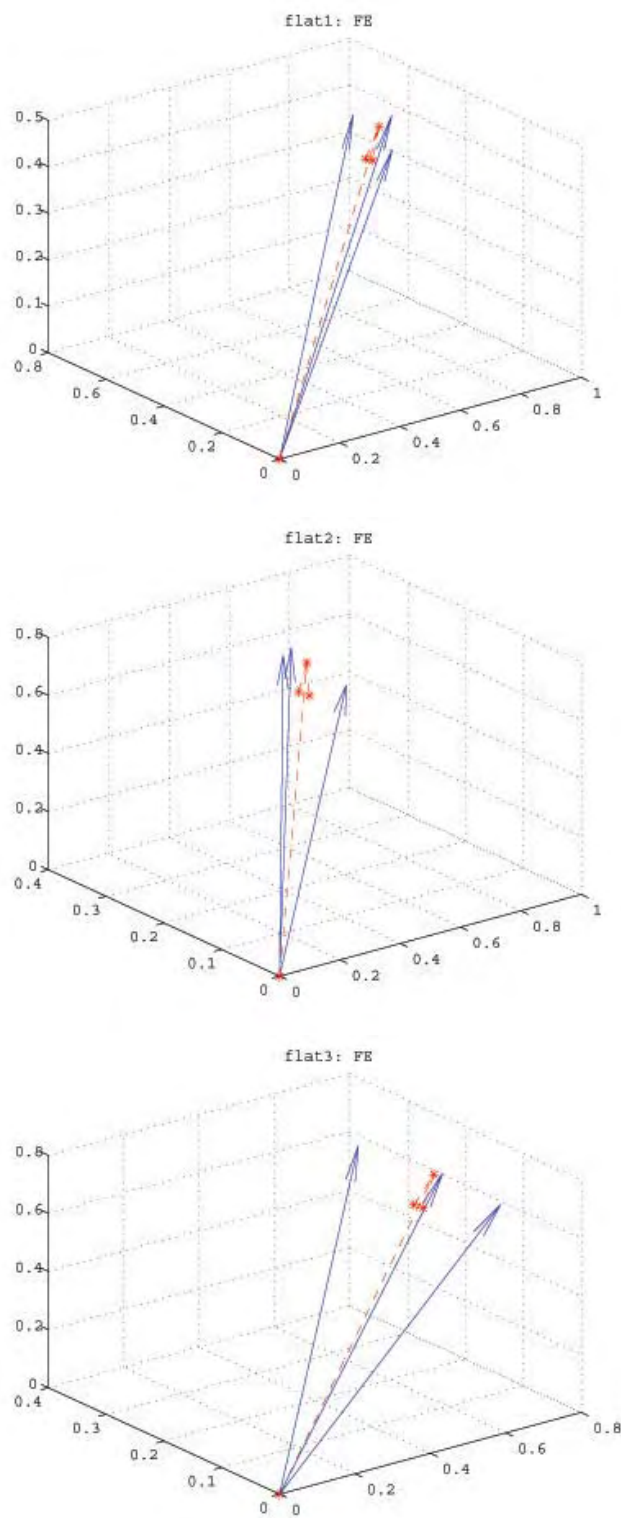


Figure 3.8: Normals for flat and their respective average in dashed line, FE

Chapter 3. Comparison between FD and FE

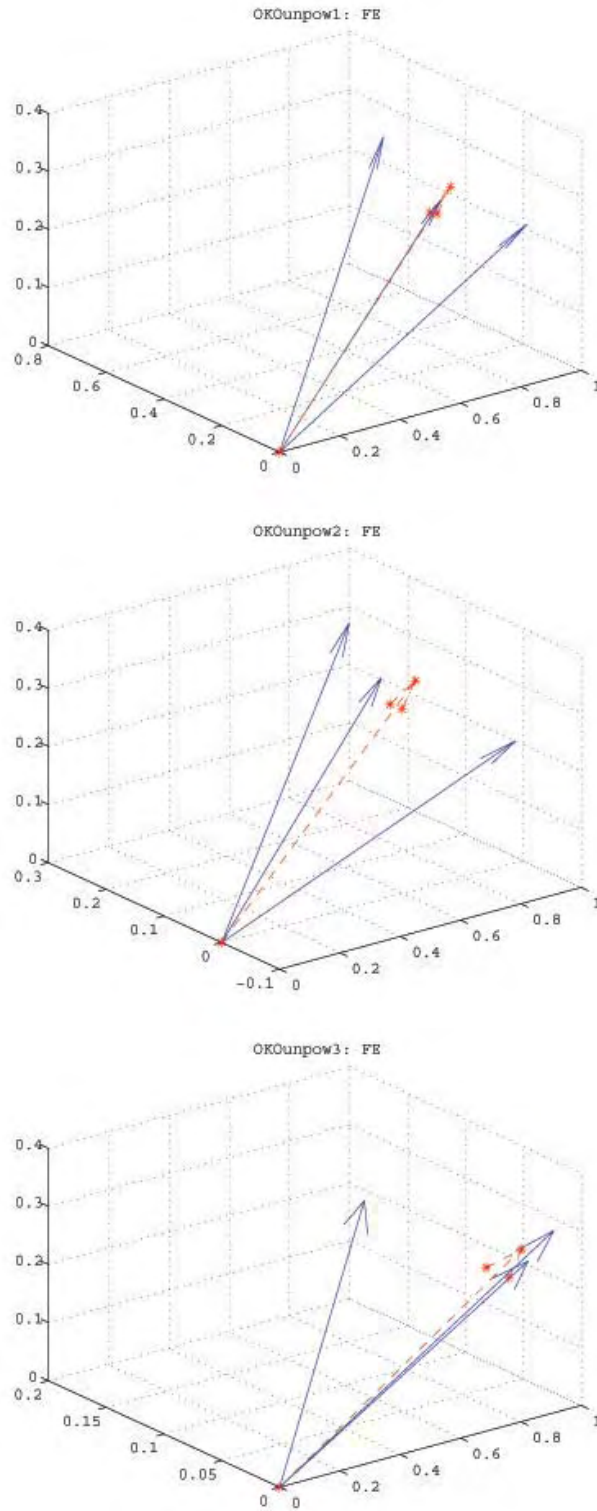


Figure 3.9: Normals for OKOunpow and their respective average in dashed line, FE

Chapter 3. Comparison between FD and FE

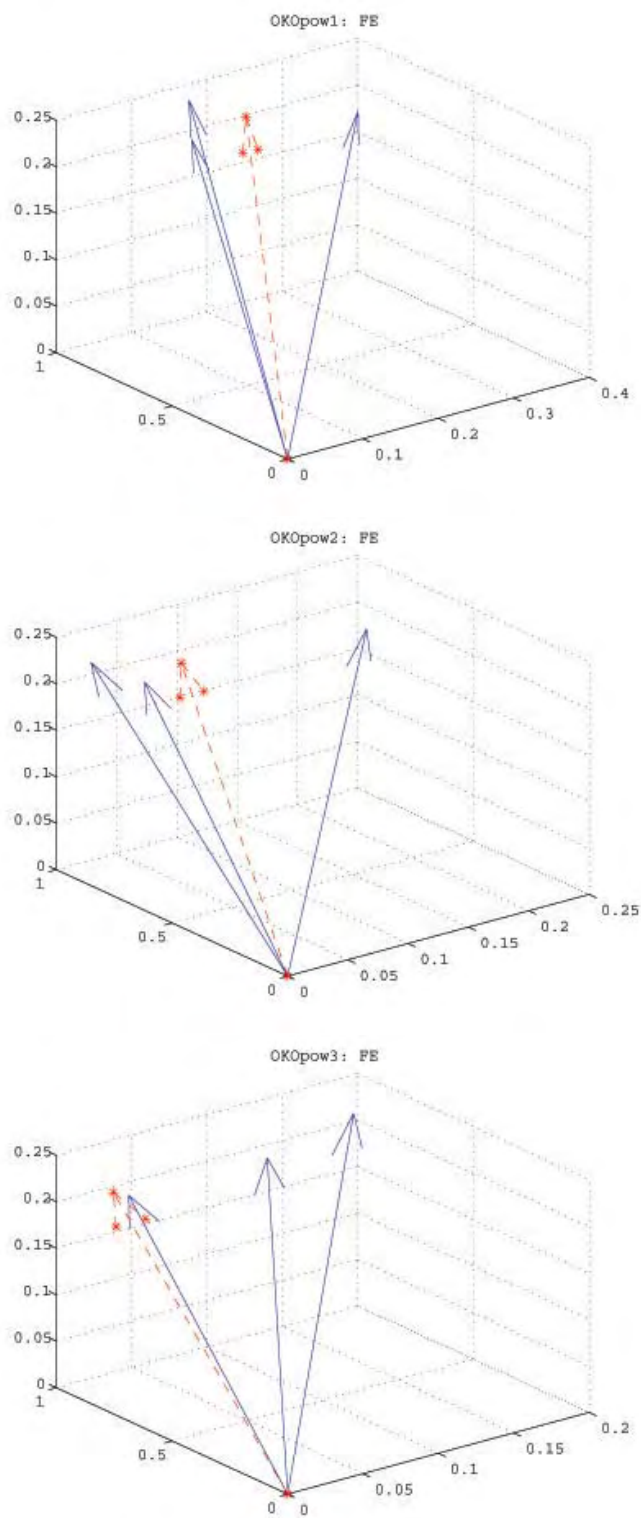


Figure 3.10: Normals for OKOpow and their respective average in dashed line, FE

Chapter 4

Vibration testing of a 16” Composite Material Telescope

The undesired motion of the telescope structure which may be induced by ground vibrations, the tracking mechanism or wind shake, results in degradation of the output wavefront. This chapter focuses on finding three principal characteristics of the resulting vibrations: the amplitude, the frequency and the damping ratio.

4.1 Background on Vibration Testing

A very common source of vibration test is the sudden application of an impulse. The impulse response function($h(t)$), is measured to determine the system’s properties. Consider an underdamped single-degree-of-freedom (SDOF), spring-mass system with an impact applied to it, as shown in Figure 4.1. The equation of which describes the system is obtained by applying Newton’s second law of motion, resulting in a second order linear differential equation with constant coefficients of the form,

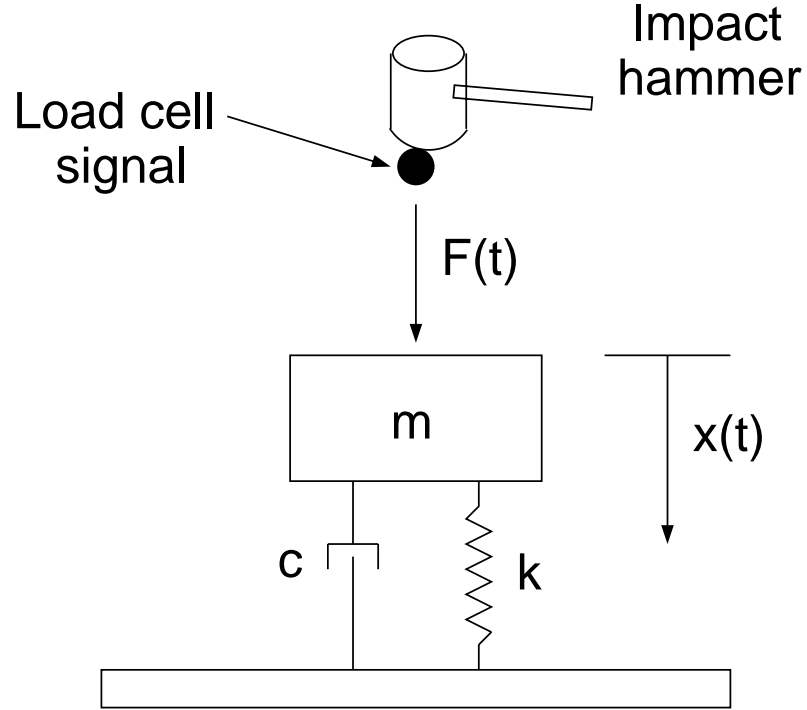


Figure 4.1: Single degree of freedom system

$$m\ddot{x} + c\dot{x} + kx = F(t) \quad (4.1)$$

where m is the mass, c refers to the damping coefficient, k the stiffness of the spring and $F(t)$ is the applied force. This differential equation of motion with constant coefficients, in reality, is only an approximation of a linear system, due to the fact that the damping and restoring forces tend to have nonlinear behavior. The general solution for equation 4.1 is given by

$$x = e^{-\alpha t}(A\cos(\gamma t) + B\sin(\beta t)) \quad (4.2)$$

Chapter 4. Vibration testing of a 16" Composite Material Telescope

where A and B are the constant coefficients, γ and β are the frequencies and α is the damping coefficient. Thus the response of an impulse applied to a SDOF underdamped system results

$$x(t) = \frac{\hat{F}e^{-\alpha t}}{m w_d} \sin w_d t \quad (4.3)$$

where \hat{F} is the impulse function, m the mass, w is the natural frequency and w_d is the damped natural frequency. The response of the system, $x(t)$, will have a form similar to the one shown in Figure 4.2. An important characteristic of this equation is that the vibrations, decays within the exponential envelope function $e^{-\alpha t}$ and from this function it can be obtained the damping coefficient and the approximate relaxation time, or effective time for which the damping of the structure minimize, $t_{damping} \approx \frac{1}{\alpha}$.

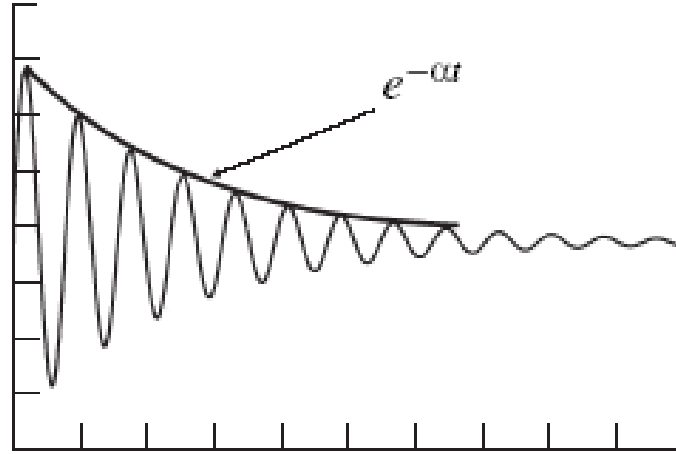


Figure 4.2: Theoretical damped vibration response of a structure

Rewritten equation 4.3 in a more convenient way so that the impulse response function can be seen,

$$x(t) = \hat{F}h(t) \quad (4.4)$$

Chapter 4. Vibration testing of a 16" Composite Material Telescope

where $h(t)$ is given by

$$h(t) = \frac{1}{mw_d} e^{-\zeta \omega t} \sin \omega_d t \quad (4.5)$$

Equation 4.5 refers to the response of a unit impulse, or $\delta(t)$, applied at $t = 0$. If it is applied at a different time, $t = \tau$, it can be written as

$$h(t - \tau) = \frac{1}{mw_d} e^{-\zeta \omega (t - \tau)} \sin \omega_d (t - \tau) \quad (4.6)$$

The response of a system, Figure 4.2, can be used to obtain the damping ratio from the value of the logarithmic decrement, δ [30][31]. The δ can be calculated by equation 4.7.

$$\delta = \ln \frac{x(t)}{x(t + T)} \quad (4.7)$$

If the value of the system response, $x(t)$, is measured at any two successive peaks, $x(t)$ and $x(t + T)$, where T is the period of oscillation, the δ can be calculated and from this the damping ratio by

$$\alpha = \frac{\delta}{\sqrt{4\pi^2 + \delta^2}} \quad (4.8)$$

The theoretical model presented above demonstrates, how to obtain the vibrations parameters from the response of a structure, meaning that by applying an impulse to the structure under test, in this case the CFRP telescope structures, the parameters can be measured.

4.2 Experimental description and results

Vibration experiments require an exciter, transducer, amplifier and a data acquisition system. For modal testing there are two main types of exciter which are shaker (electromagnetic or electro hydraulic) and impulse hammers. Due to the simplicity over shaker, the selected exciter for this type of test was the impulse hammer.

Chapter 4. Vibration testing of a 16" Composite Material Telescope

A common impulse hammer, also known as impact hammer, consists of a hammer with a force transducer built into the head of it. This hammer hits the structure under test, exciting a broad range of frequencies. A modified version of an impact hammer was used to excite the telescope structure. The impact mass which provided the impulse of the telescope structure was a pendulum system, as shown in Figure 4.3 and Figure 4.4, consisting of a lead mass attached to fishing line. This impacted the telescope structure at the bottom of the mirror cell.

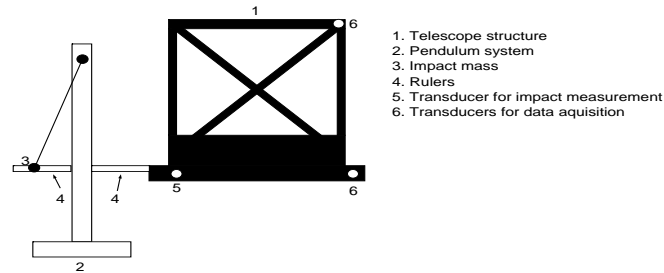


Figure 4.3: Drawing of the set-up of the vibration test experiment showing the impact weight structure and position of the accelerometers.

Three accelerometers were placed at specific locations on the telescope structure, as seen in Figure 4.3. Two of the accelerometers were connected to a computer based oscilloscope system for data acquisition. Figure 4.5(a) shows the position of the accelerometers, one was placed in the top, marked as **A1** which corresponds to the top accelerometer and channel 1 of the oscilloscope, the second was placed at the bottom base, marked as **A2** which corresponds to the bottom accelerometer and channel 2 of the oscilloscope. The extra accelerometer, placed at the position marked as **A**, was connected to an external oscilloscope which allowed qualitative tracking of the impulse applied to the mount, to ensure it was as repeatable as possible.



Figure 4.4: Pendulum system which provided the impulse or impact on the structure.

A general picture of the complete system set-up with the accelerometers in place and the oscilloscopes is shown in Figure 4.5(b).



(a) Position of the accelerometers marked as **A**, **A1** and **A2**



(b) Experimental set-up showing the oscilloscope, accelerometer and impact hammer set-up

Figure 4.5: (a)Shows the accelerometers position, CH1 being the top accelerometer and CH2 the bottom or base accelerometer.(b)Complete set-up of the experiment.

Other than the extra accelerometer positioned for tracking the impulse applied, a set of two rules, were used to maintain a constant distance from the telescope point of impact to the rest position. They also calibrated the displacement of the pendulum before applying the impulse. This modified impact hammer set-up allowed the application of a more or less constant impulse to the structure.

4.2.1 Data acquisition

The complete set of measurements was divided in two main categories, measurements inside and outside. Inside referring to measurements performed indoors, where the external vibrations sources are minimal. Outside, meaning measurements performed with the telescope structure in the open, exposed to external vibrations sources, mainly and most noticeable the wind. Also the measurements were divided into measurements done with the telescope and mount on the floor and measurements on the tripod. The following list represents the data acquisition procedure performed:

- Measurements inside:
 - Without tripod: These measurements were performed with the telescope fork base at the floor, at two different angles; 0° from zenith and 45° from zenith, Figure 4.6.

Of the experimental measurements listed, it was chosen to analyze in detail the inside 0° set only, in order to explore the most effective data reduction protocol. The pictures in Figure 4.6, shows the example of a general data acquisition procedure; inside, without tripod and at the three different angles.

Chapter 4. Vibration testing of a 16" Composite Material Telescope



(a) Telescope at 0°



(b) Telescope at 45°

Figure 4.6: Telescope measurements at different angles performed inside

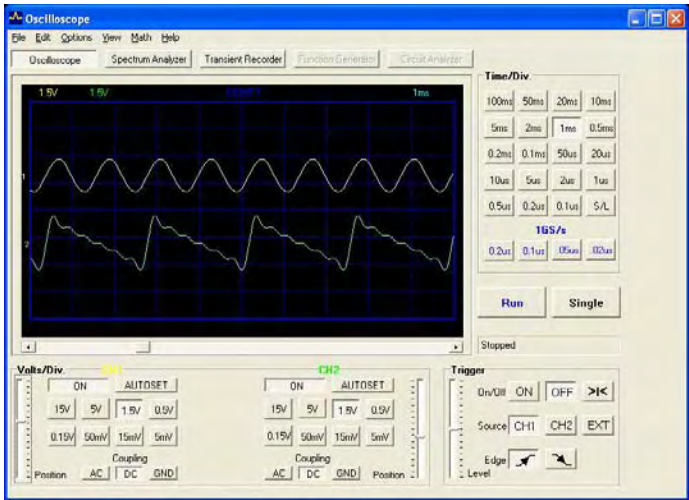
The data was saved as a text file into a computer using the computer based oscilloscope¹. The text file contains:

- Starting and stopping time of the measurement
- Time and voltage step
- Number of samples
- Data from each of the channels in use

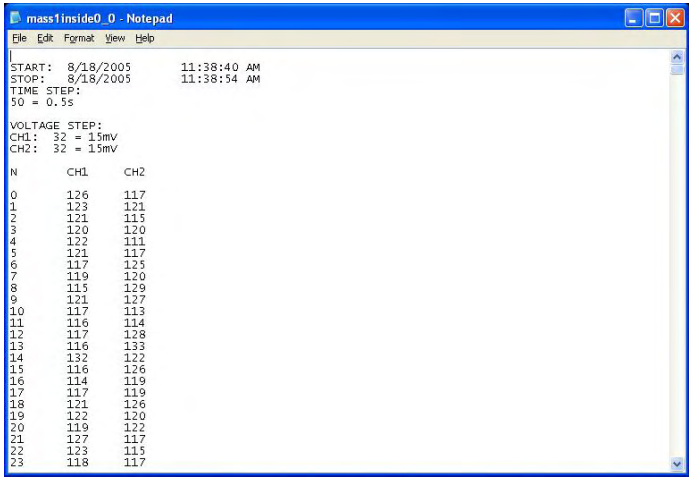
Figure 4.7(a) shows the user interface of the oscilloscope and Figure 4.7(b) shows the general output text file obtained from it.

¹Oscilloscope model: Velleman PC oscilloscope PCS500

Chapter 4. Vibration testing of a 16" Composite Material Telescope



(a) Oscilloscope, Graphical User Interface(GUI)



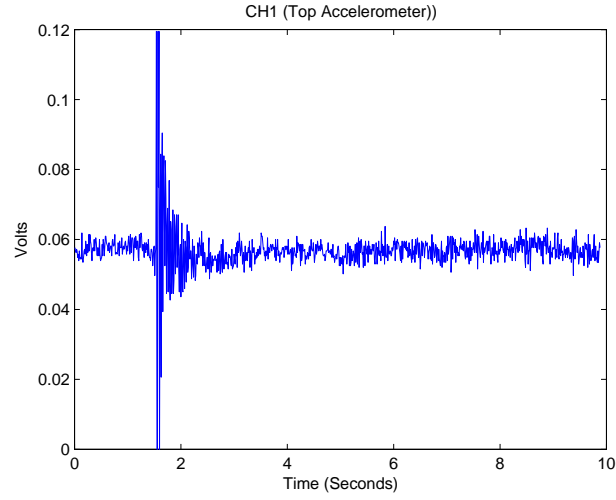
(b) Output text file

Figure 4.7: Oscilloscope GUI and output file sample

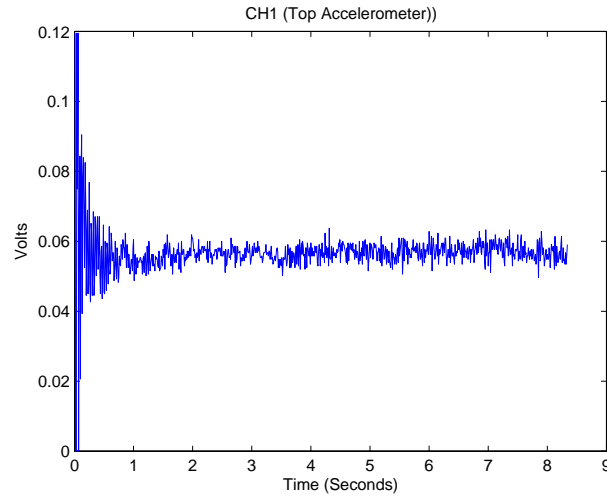
Chapter 4. Vibration testing of a 16" Composite Material Telescope

A Matlab code was written to read the data for analysis, Figure 4.8 shows a sample of the data obtained from a measurement performed inside, with Figure 4.8(a) being the raw signal obtained from the oscilloscope, with approximately a second before the impulse is applied to the structure. Figure 4.8(b) shows the cropped data prior to the data reduction process.

Chapter 4. Vibration testing of a 16" Composite Material Telescope



(a) Signal not modified



(b) Signal modified

Figure 4.8: (Top:) Signal recorded from the oscilloscope with approximately a second of readout noise before the impact. (Bottom:) Modified signal for data analysis.

4.2.2 SDOF fitting analysis and results

Taking into account the superposition principle the curves used to fit the data ranges from analytical functions of the form

$$Fit_{func} = Ae^{-\alpha t} \Rightarrow Fit_{func} = Ae^{-\alpha t} [B\sin(\beta t) + C\cos(\gamma t)] + D \quad (4.9)$$

where A is the magnitude of the oscillation, α is the damping coefficient, β and γ are the frequencies and D is the intercept in the volt axis. Figure 4.9 shows the fit for a set of data for CH1(Top accelerometer) and CH2(Bottom accelerometer) for the telescope at zenith.

Chapter 4. Vibration testing of a 16" Composite Material Telescope

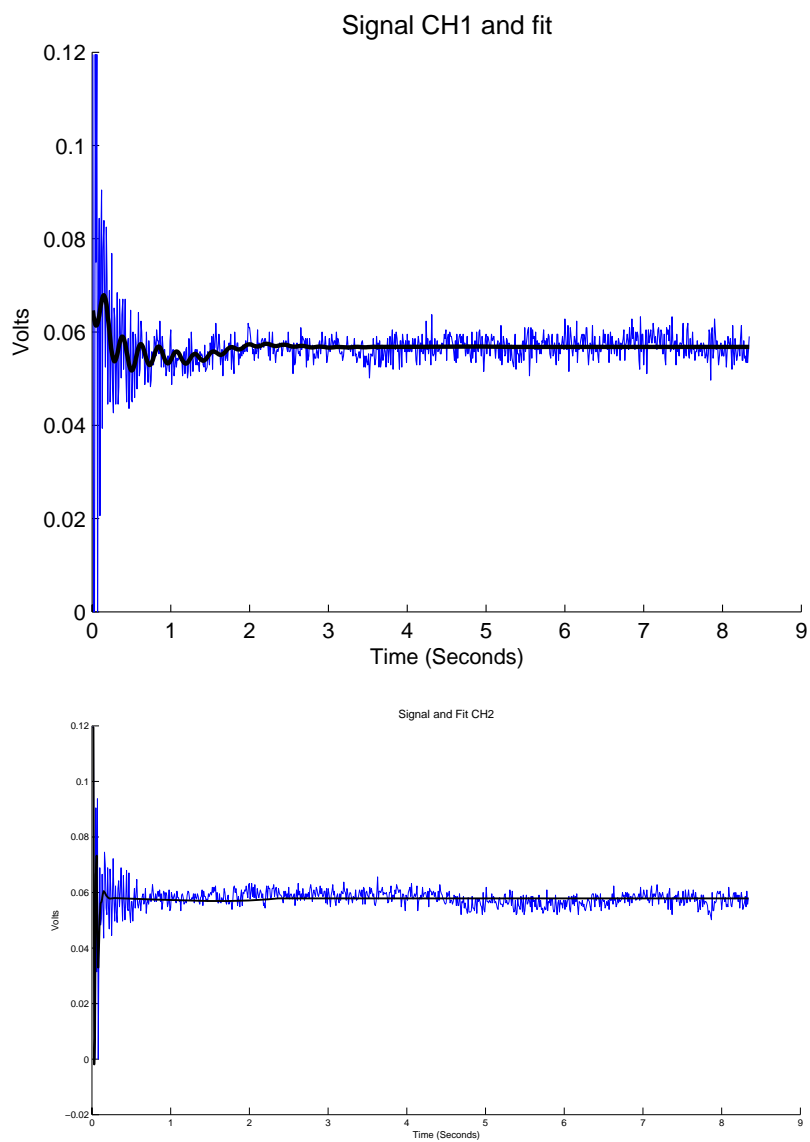


Figure 4.9: (Top:)Signal from CH1 and the fitted function for it. (Bottom:)Signal from CH2 and the fitted function for it.

Chapter 4. *Vibration testing of a 16" Composite Material Telescope*

From the fit the decaying envelope function was obtained, Figure 4.10-4.10.

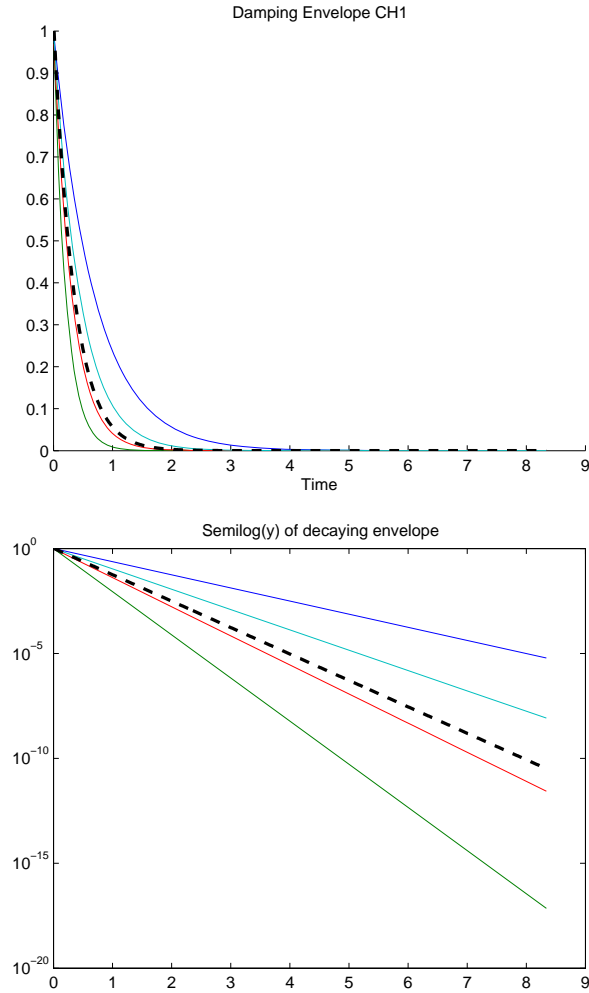


Figure 4.10: (Top:)Decaying envelope fit for CH1 & (Bottom:) CH2 for the telescope at zenith.

Chapter 4. Vibration testing of a 16" Composite Material Telescope

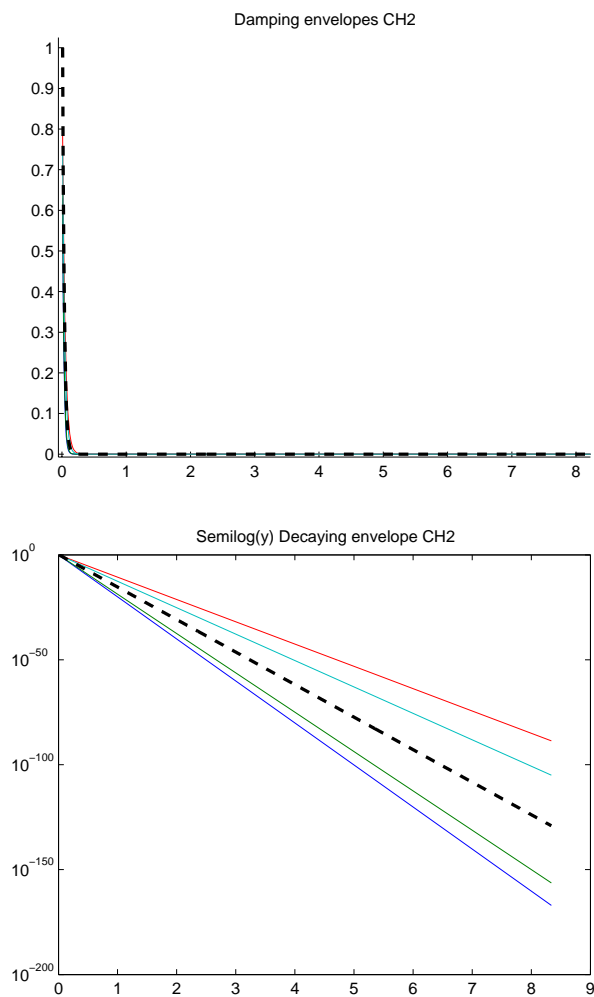


Figure 4.11: (Top:)Decaying envelope fit for CH1 & (Bottom:) CH2 for the telescope at zenith.

Chapter 4. Vibration testing of a 16" Composite Material Telescope

The Power Spectrum(PS) was calculated for both channels in order to find the signal power density at a specific frequency. Figure 4.12 shows the PS for CH1, also with its logarithmic plot in order to emphasize small amplitude details in the signal. Both PS plots clearly show that there is a strong signal at approximately 30 Hz and the cut-off frequency at approximately 15Hz.

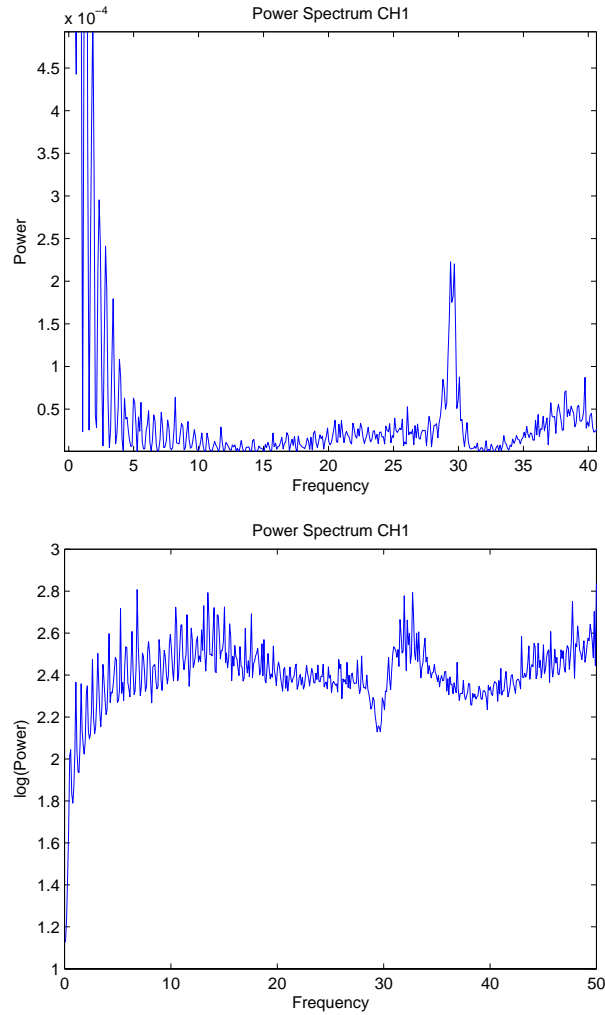


Figure 4.12: (Top:)Power spectra & (Bottom:) Log plot of the power spectra for CH1

The same plots are shown in Figure 4.13 for CH2. Both plots for this channel

Chapter 4. Vibration testing of a 16" Composite Material Telescope

does not gave much information about the frequency power of the signal.

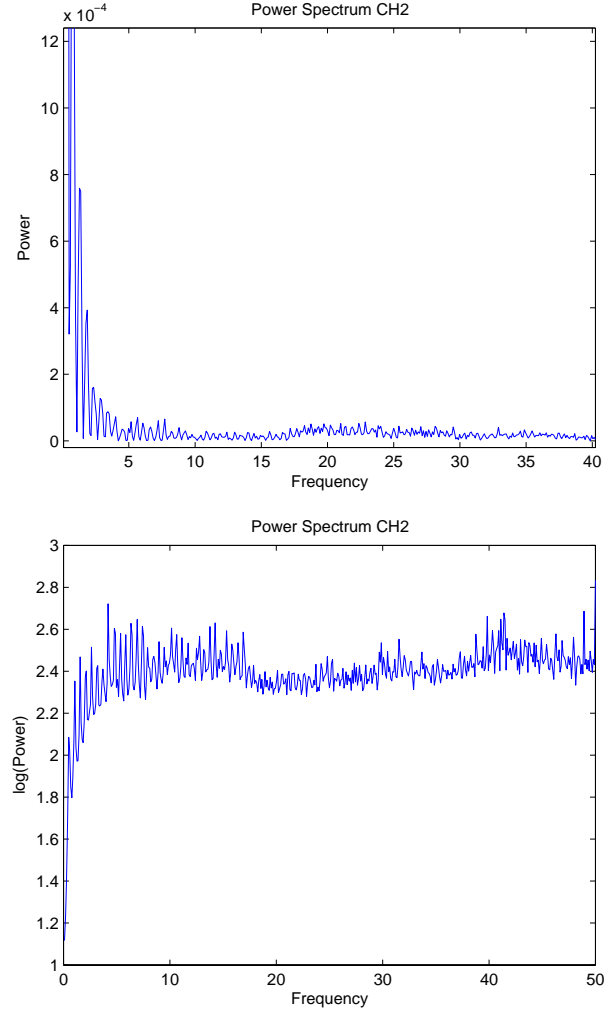


Figure 4.13: (Top:)Power spectra & (Bottom:) Log plot of the power spectra for CH2

Table 4.1 shows parameters obtained from the fitted functions and from Fourier analysis. The three important parameters from this table are the damping ratio, cut-off frequency and the effective time; evidently further refinement is needed for the data analysis procedure since the SDOF fit is not highly reliable for CH2.

Table 4.1: Parameters obtained from the decaying enveloped fit using Fourier analysis on the modified signal.

Vibration Paramters for CH1 & CH2 with telescope at zenith		
Parameter	CH1(units)	CH2(units)
Amplitude	0.105	1.313
Damping ratio	2.900	5.305
Effective time	0.344 s	0.188 s
Cut-off frequency	15 Hz	14 Hz
Natural frequency	9.217	49.889

By Fourier analysis only CH1 shows a strong signal structure, but little was seen for CH2. Also there is no easy way of extracting noise from the signal and knowing the direction of the vibrations induced from the impulse. Another technique, Empirical Mode Decomposition (EMD), was implemented in order to analyze the vibration data from the telescope, described in the next section.

4.2.3 Empirical Mode Decomposition (EMD)

Empirical Mode Decomposition is a new method introduced by Huang(1996)[32] for analysing nonlinear, non-stationary data². This method provides the tools for decomposing any complicated data set into a finite number of *intrinsic mode functions* (IMFs) that admit well-behaved Hilbert transforms. The IMFs resulting from the EMD are sifted with respect to their instantaneous frequency.

The main idea behind the method is summarized in Figures 4.14-4.17, which shows the sifting process. The sifting process consists of decomposing the signal, first selecting the maxima and the minima of the signal, performing an average between the two and subtracting the results from the original signal. This procedure

²Stationary data approximately means that the mean of a subset of a data series equals the mean of the whole series

is iterated to zero the mean, resulting in a number of IMFs.

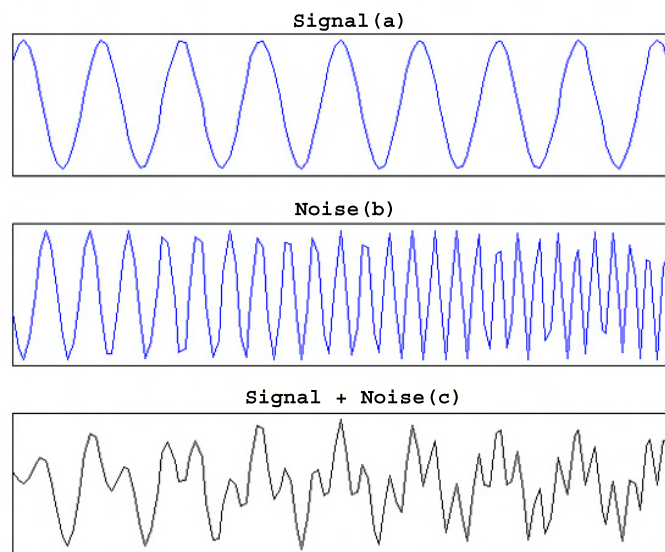


Figure 4.14: (a)Signal. (b)Noise. (c)Signal embedded in noise.

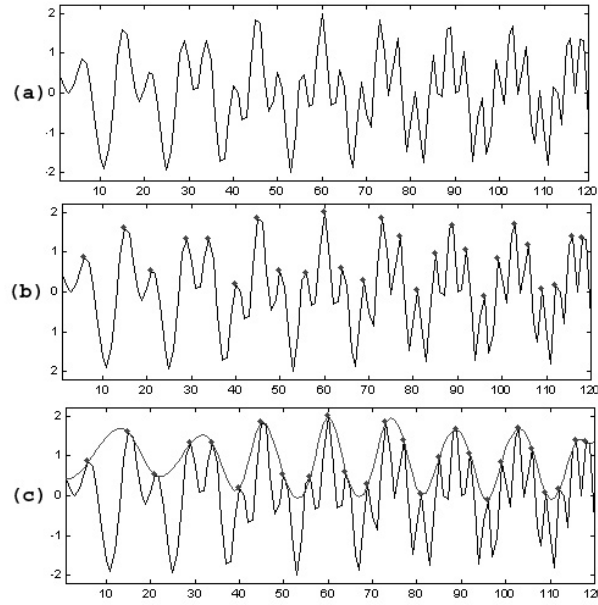


Figure 4.15: (a)Signal and noise. (b)Selection of local maxima for the complete data.(c)Envelope of the selected maximas.

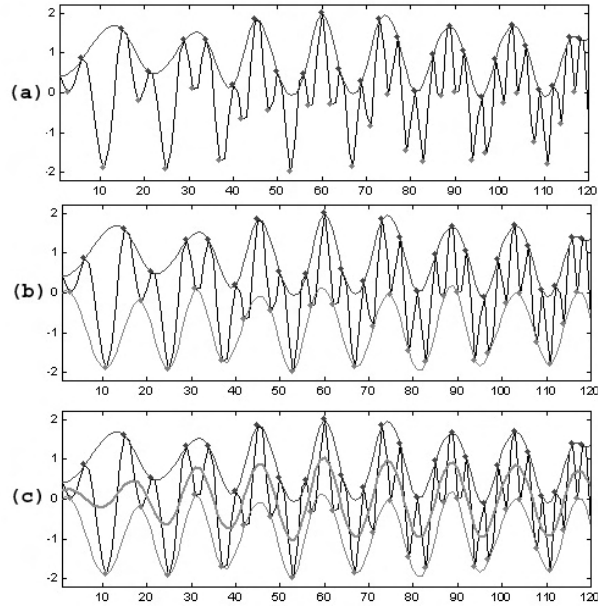


Figure 4.16: (a)Selection of local minima. (b)Envelope of the minima.(c)The mean between the upper and lower envelopes.

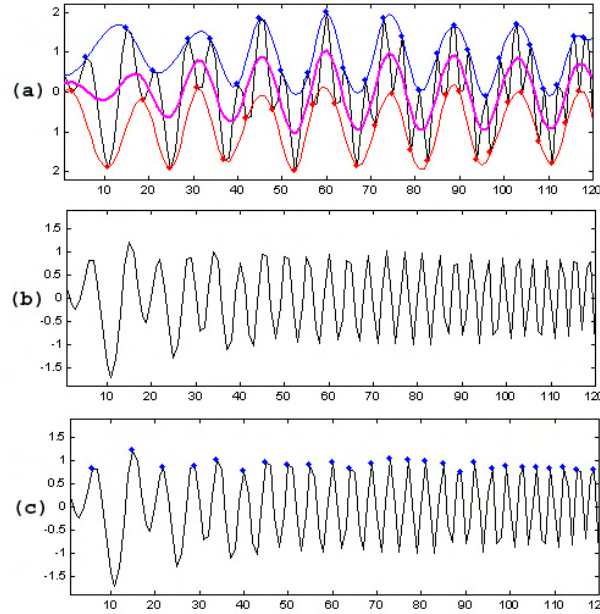


Figure 4.17: (a)Mean between the envelopes. (b)Residue. (c)This is the first intrinsic mode function(IMF). Start at the First step.

4.2.4 Results

Results are shown in this section by using the EMD method in the data obtained from the accelerometers. The codes were developed by G. Rilling and the Hilbert transform was an in house tool from the University of Puerto Rico, Mayagüez Campus, Optics Lab. By using EMD the intrinsic mode functions were obtained for the data from each channel, as seen in Figures 4.18 and 4.19. The sifting process works as a filter back, by decomposing the signal from the accelerometers. It seems that the first three IMFs mainly contain the impulse signal, the next IMFs possibly contain the noise from accelerometers or surroundings ambient and the residual contains the trend line which is related to the accelerometers' read-out voltage range.

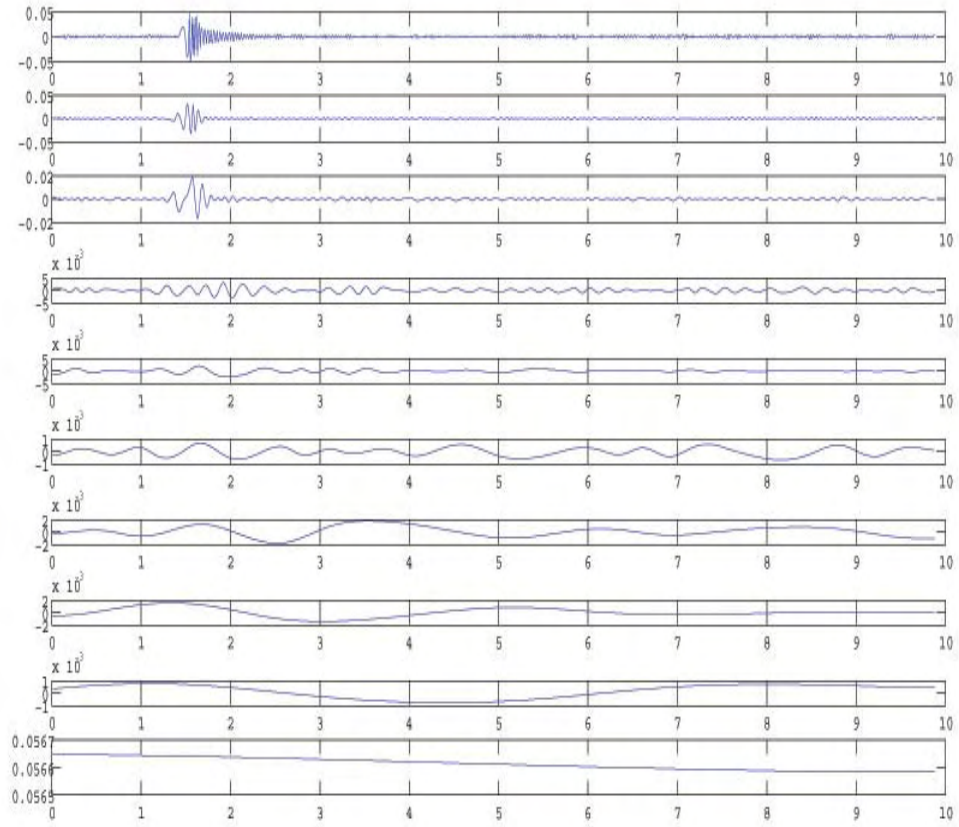


Figure 4.18: CH1: From top to bottom: The first three IMFs contains the signal strenght. The next three IMFs contains structure which may be related to signal and propagation of it on the structure. The next three contains the noise from the ambient and the accelerometers. The last IMF is the trend line.

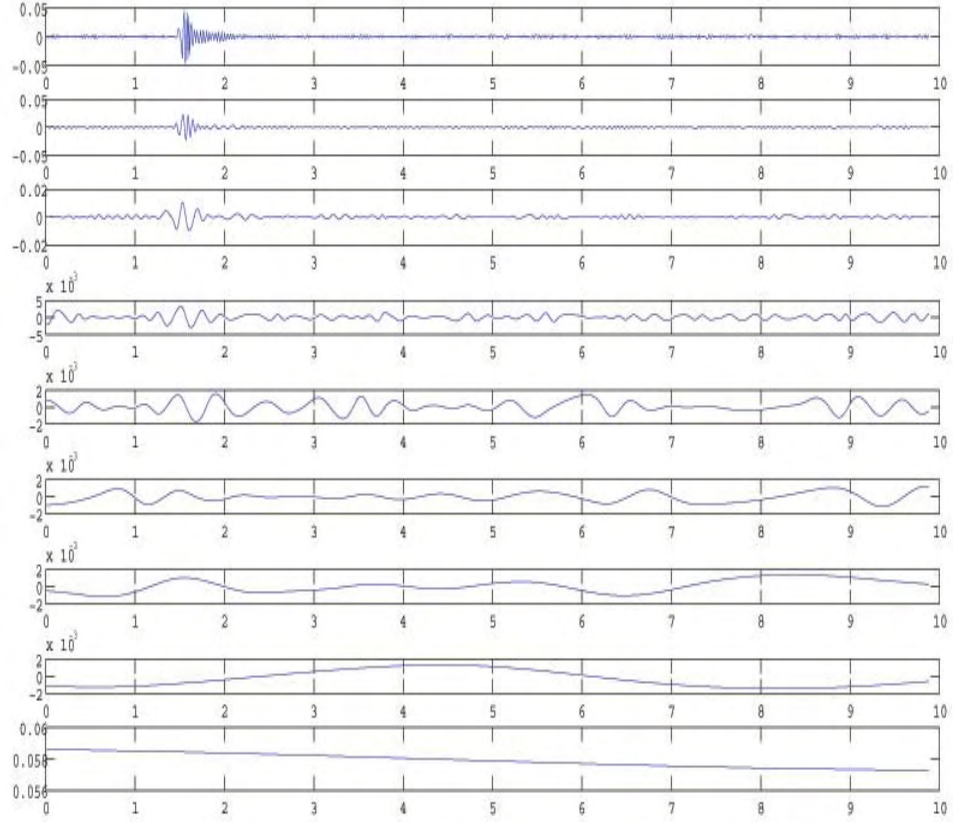


Figure 4.19: CH2: From top to bottom: The first three IMFs, contains the signal strenght. The next two IMFs, contains structure which may be related to signal and propagation of it on the structure. The next three contains the noise from the ambient and the accelerometers. The last IMF is the trend line.

An advantage of the IMFs is that they allow to define a physical phase angle from a real signal, through the use of the Hilbert transform[33][34]. This is done through the analytic signal[35],

$$Z(t) = X(t) + iY(t) \quad (4.10)$$

where $X(t)$ is the signal and $Y(t)$ is the Hilbet transform of the signal, so the phase

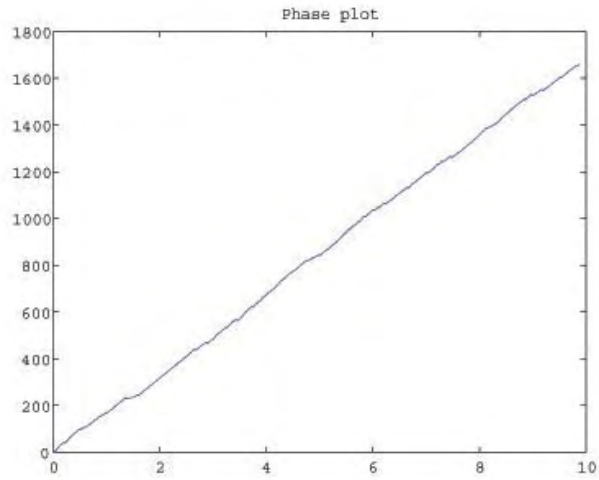
angle is

$$\theta(t) = \text{atan} \frac{Y(t)}{X(t)} \quad (4.11)$$

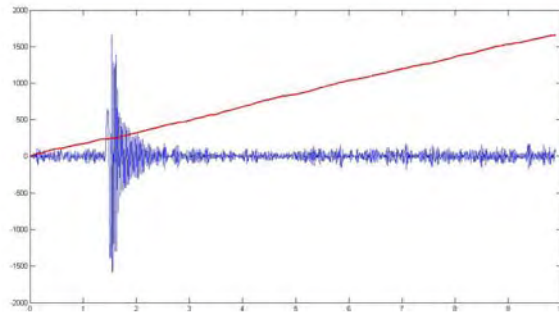
Taking as an example data from CH1, it was investigated the phase angle derived from IMF1 in Figure4.20. The phase plot allows for an identification point of the impact time on the structure, identified by the sudden change in the slope of the phase plot. Also the amplitude of the analytic signal is defined through,

$$Amp = (X(t)^2 + Y(t)^2)^{(1/2)} \quad (4.12)$$

which is shown in Figure4.21. Assuming IMF1 is solely the impulse signal a fit of a decayin envelope function can be made.

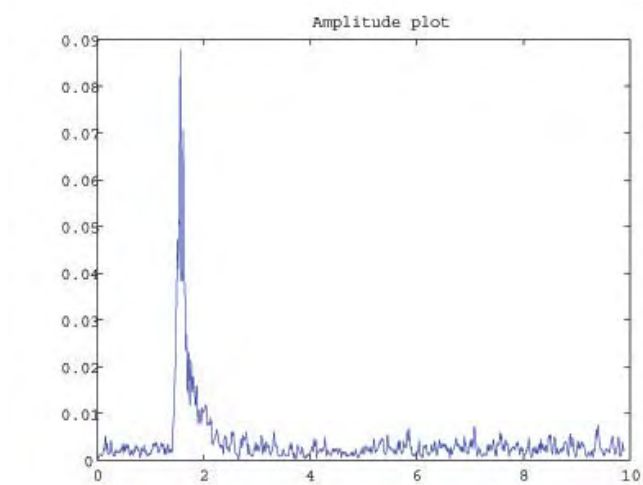


(a) Phase angle information from Hilbert transform of IMF1 for CH1.

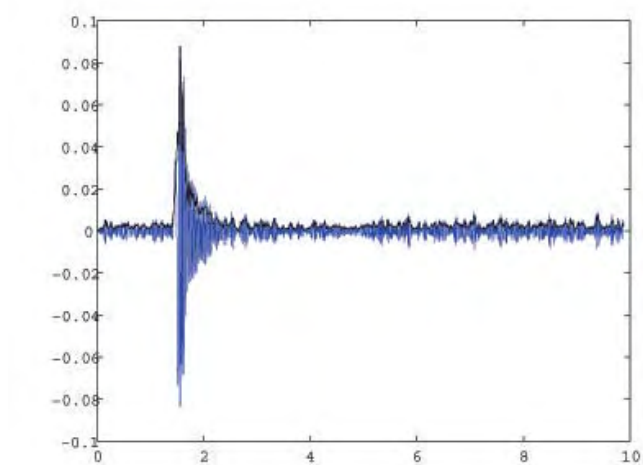


(b) Overplot of signal from CH1 and phase angle.

Figure 4.20: Phase angle plots for CH1.



(a) Amplitude from Hilbert transform of IMF1 for CH1.

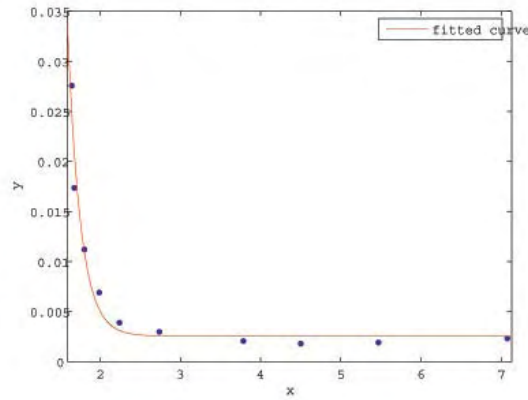


(b) Overplot of the signal from CH1 and its amplitude.

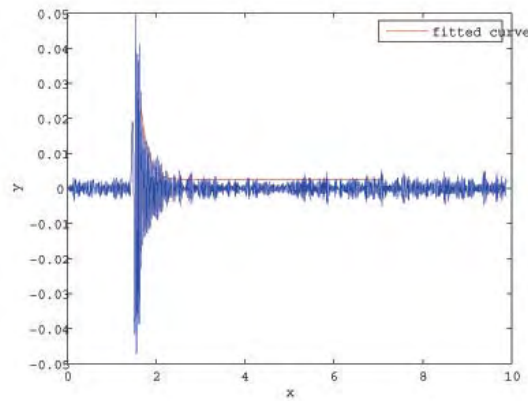
Figure 4.21: Amplitude plots for CH1.

Chapter 4. Vibration testing of a 16" Composite Material Telescope

From EMD results for CH1 the first IMF(IMF1), was taken as the new signal and a decaying enveloped function was fitted to it, Figure 4.22, in order to obtain parameters such as: maximum amplitude, damping ratio, logarithmic decrement, effective time of damping and an estimate of the natural frequency of the system. Table 4.2 shows these values. The three important parameters from this table are the damping ratio, cut-off frequency and the effective time.



(a) Points used for fitting the envelope.



(b) Signal and the fitted decaying function on top.

Figure 4.22: Decaying fit made for IMF1 from the telescope at zenith.

Table 4.2: Parameters obtained from the decaying enveloped fit

Vibration Paramters for CH1 & CH2 with telescope at zenith		
Parameter	CH1(units)	CH2(units)
Amplitude	596.2683	10254
Damping ratio(calculated)	0.0736	0.0746
Logarithmic decrement(calculated)	0.4639	0.4698
Effective time	0.1613 s	0.1206 s
Cut-off frequency	10 Hz	10 Hz
Natural frequency	84.1743	111.23

Applying Fourier analysis to IMF1 of both CH1 & CH2 for the 0° indoor dataset, it is seen that the low frequency component have been suppressed. Figure 4.23 agrees with figure 4.12 in that there is a strong 30 Hz component. However, Figure 4.24 shows a 30 Hz component missed off in Figure 4.13 for CH2. The filtering properties of EMD are evidently useful for improving the signal to noise ratio dramatically. Further results for other configurations are shown in Appendix **A**.

Chapter 4. Vibration testing of a 16" Composite Material Telescope

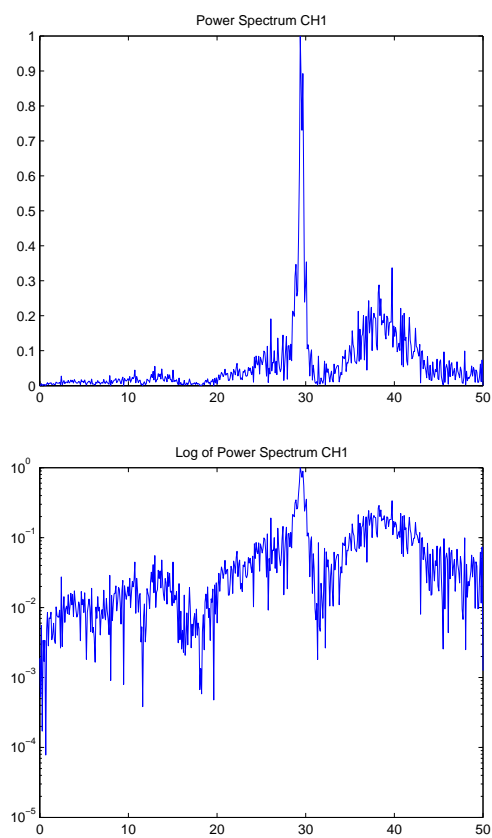


Figure 4.23: PS calculated from IMF1 for CH1.

Chapter 4. Vibration testing of a 16" Composite Material Telescope

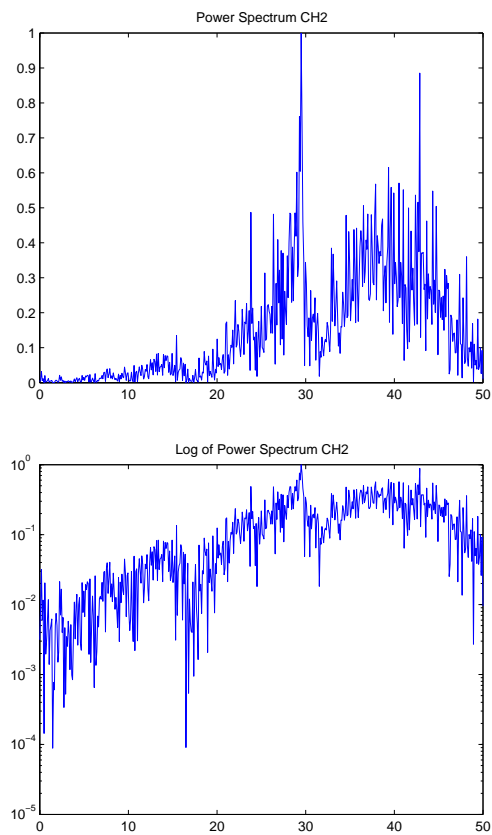


Figure 4.24: PS calculated from IMF1 for CH2.

Chapter 5

Conclusions

Work was performed on key aspects of instrumentation for image formation, specifically for an new Adaptive Tip/Tilt mirror for an Adaptive Optics(AO) system and a CFRP telescope. A wavefront reconstructor based on Finite Difference was developed for the used on square grid lenslet array Shack-Hartmann Wavefront Sensor. A second reconstructor based on Finite Element which was developed for the HOPA experiment was implemented in order to verify the results from the FD reconstructor. The reconstructor results showed that the global tip/tilt induced on the Adaptive Tip/Tilt mirror does not seem to affect the DM surface, meaning that angular tilt can be corrected by the stage, while higher order aberrations can be corrected by the DM simultaneously. Also by Table 3.1 it was shown the repitability of the tip/tilt stage, maintaining almost a constant global tilt on the wavefront[36][37].

An impulse test on the CFRP telescope structure allowed the calculation of important vibration paramaters such as damping coefficient and relaxation time. Both of these parameters are very important for imaging and real time corrections in the wavefront. The relaxation time obtained, ranged from 0.12 – 0.34 seconds meaning that even though it is a light weight structure it settles down quickly. These time

Chapter 5. Conclusions

results mean that structure vibrations can be easily corrected by an active control system. Also, the new analysis method implemented, Empirical Mode Decomposition, proved to be a useful tool for analysing further vibration data. A peak intensity at approximately 30 Hz in the frequency spectrum was clearly identify by Fourier analysis and EMD, but EMD showed that by decomposing the signal into its IMFs, and removing the noise, more details were revealed. This peak intensity was identify as the impulse applied to the structure[38][39].

Appendices

A EMD results

1

Appendix A

EMD results for telescope at 45° from zenith

Results for the configuration of the telescope at 45° from zenith:

- IMF, Figure A.1 & A.2
- Phase, Figure A.3 & A.5
- Amplitude, Figure A.4 & A.6
- Decaying Envelope, Figure A.7 & A.8
- Table of parameters, Table A.1

These results were analyzed with the same procedure as for the telescope at 0° .

□

Appendix A. EMD results for telescope at 45° from zenith

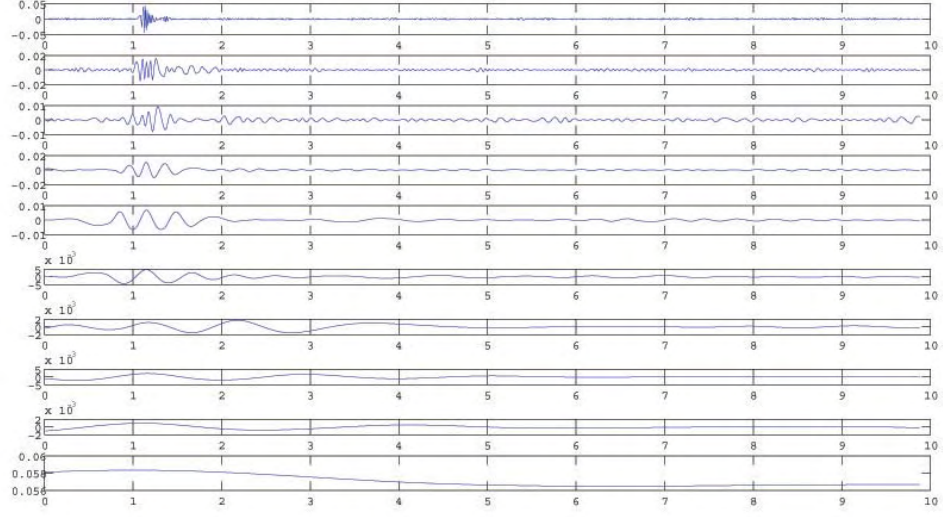


Figure A.1: IMF's for CH1 at 45° from zenith

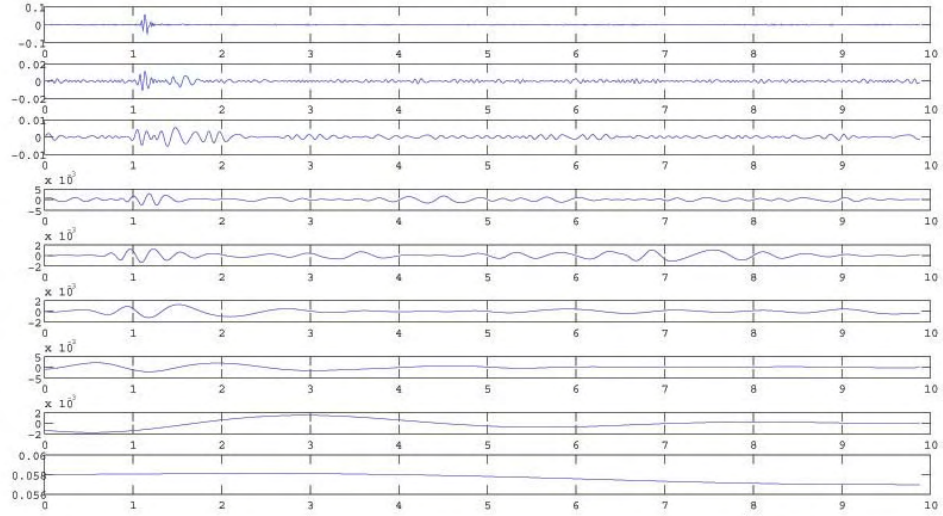


Figure A.2: IMF's for CH2 at 45° from zenith

Appendix A. EMD results for telescope at 45° from zenith

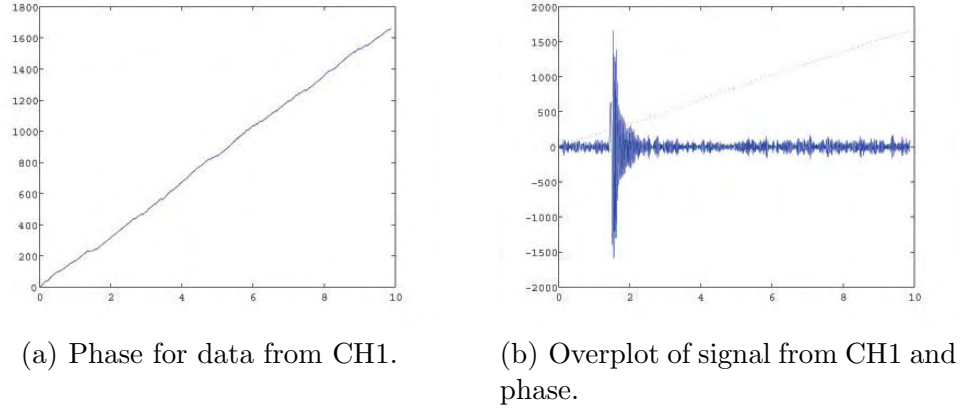
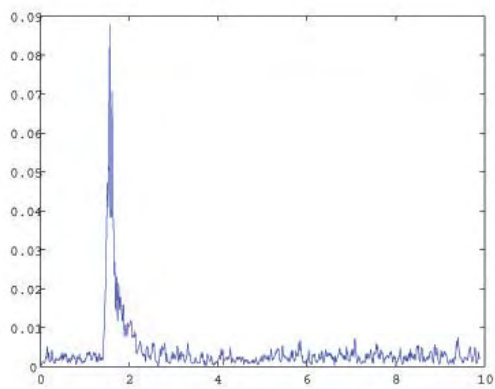


Figure A.3: Phase plots for CH1 at 45° from zenith.

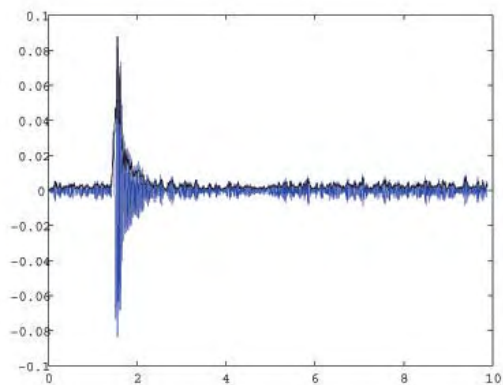
Table A.1: Parameters obtained from the decaying enveloped fit

Vibration Paramters for CH1 & CH2 with telescope at 45° from zenith		
Parameter	CH1(units)	CH2(units)
Amplitude	166.429	6434
Damping ratio(calculated)	0.0476	0.1221
Logarithmic decrement(calculated)	0.2959	0.7731
Effective time	0.1606	0.0958
Natural frequency	132.34	85.4815

Appendix A. EMD results for telescope at 45° from zenith



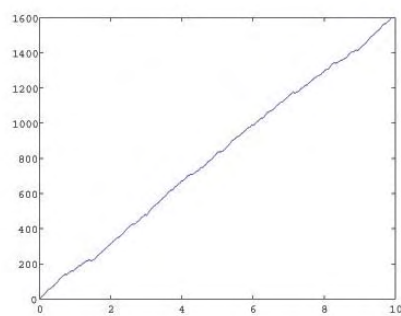
(a) Amplitude of the signal.



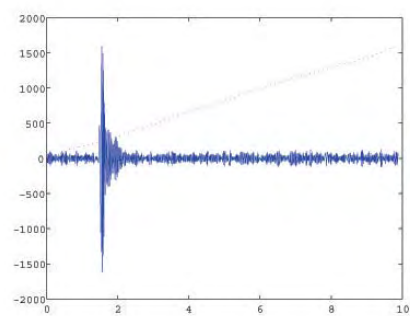
(b) Overplot of the signal and its amplitude.

Figure A.4: Amplitude plots for CH1 at 45° from zenith.

Appendix A. EMD results for telescope at 45° from zenith



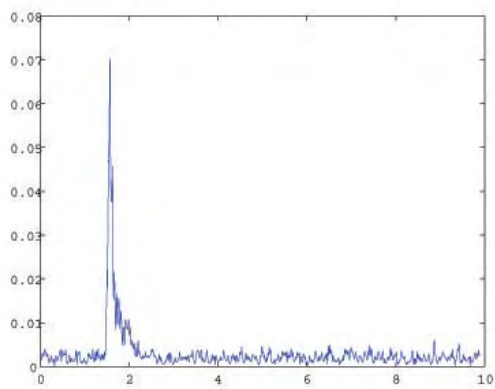
(a) Phase for data from CH2.



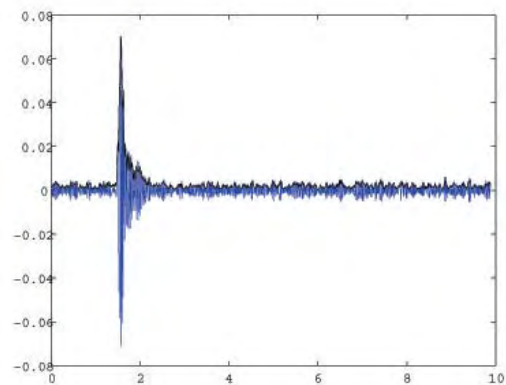
(b) Overplot of signal from CH2 and phase.

Figure A.5: Phase plots for CH2 at 45° from zenith.

Appendix A. EMD results for telescope at 45° from zenith



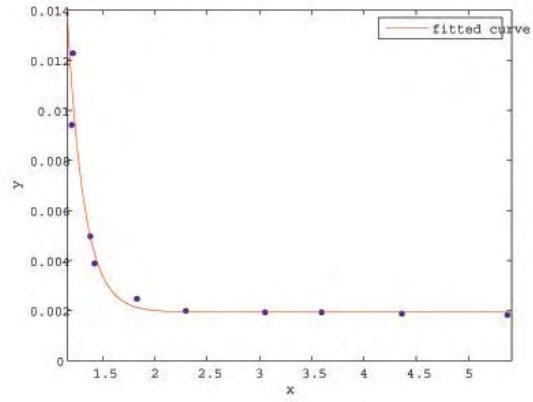
(a) Amplitude of the signal.



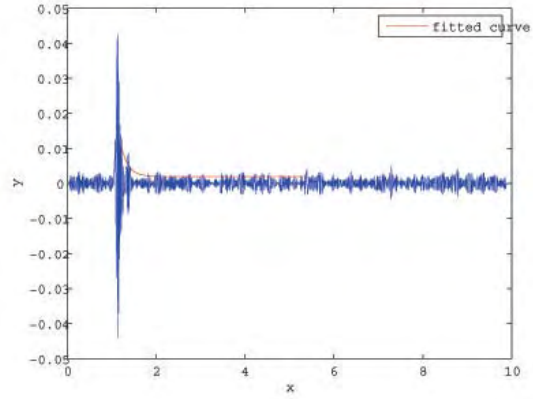
(b) Overplot of the signal and its amplitude.

Figure A.6: Amplitude plots for CH2 at 45° from zenith.

Appendix A. EMD results for telescope at 45° from zenith



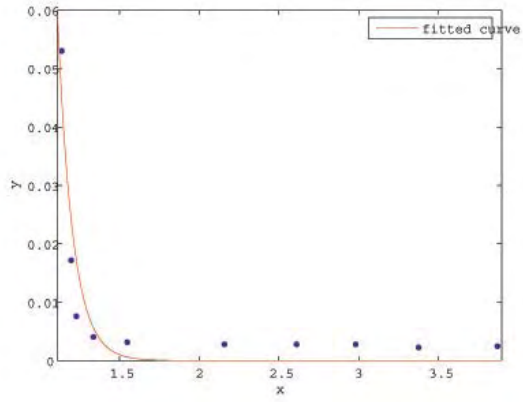
(a) Point used for the fit and the envelope.



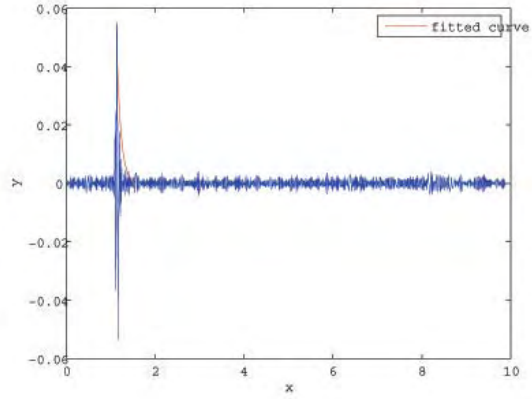
(b) Signal and the fitted decaying function

Figure A.7: Decaying fit made for the data from the telescope at 45° from zenith, CH1.

Appendix A. EMD results for telescope at 45° from zenith



(a) Point used for the fit and the envelope.



(b) Signal and the fitted decaying function

Figure A.8: Decaying fit made for the data from the telescope at 45° from zenith, CH2.

References

- [1] P. G. Tuthill, C. A. Haniff, and J. E. Baldwin, “Hotspots on late-type supergiants,” *Monthly Notices of the Royal Astronomical Society* **285**, pp. 529–539, Mar. 1997.
- [2] R. Arsenault, D. Salmon, J. Kerr, F. Rigaut, D. Crampton, and W. Grundman, “PUEO, the Canada-France-Hawaii Telescope Adaptive Optics Bonnette I: System Description,” in *Astronomy with the CFHT Adaptive Optics Bonnette*, R. Arsenault, ed., pp. 1–+, 1994.
- [3] J. W. Goodman, *Introduction to Fourier Optics*, McGraw-Hill, Boston, 1996.
- [4] R. K. Tyson and B. W. Fraizer, *Field Guide to Adaptive Optics*, SPIE Press, Washington, 2004.
- [5] L. C. Andrews, *Field Guide to Atmospheric Optics*, SPIE Press, Washington, 2004.
- [6] M. C. Roggeman and B. Welsh, *Imaging through turbulence*, CRC Press, Boca Raton, Florida, 1996.
- [7] R. Conan, A. Ziad, J. Borgnino, F. Martin, and A. A. Tokovinin, “Measurements of the wavefront outer scale at Paranal: influence of this parameter in interferometry,” in *Proc. SPIE Vol. 4006, p. 963-973, Interferometry in Optical Astronomy*, Pierre J. Lena; Andreas Quirrenbach; Eds., P. J. Lena and A. Quirrenbach, eds., pp. 963–973, July 2000.
- [8] A. Kolmogorov, “The general theory of dynamical systems and classical mechanics,” in *Proceedings of the International Congress of Mathematicians*, 1954.
- [9] V. I. Tatarskii, *The Effects of the Turbulent Atmosphere on Wave Propagation*, Keter, Jerusalem, 1971.

References

- [10] <http://www.compositemirrors.com/index.htm>.
- [11] H. W. Babcock, “The Possibility of Compensating Astronomical Seeing,” *Publications of the Astronomical Society of the Pacific* **65**, pp. 229–+, Oct. 1953.
- [12] F. Roddier, *Apaptive optics in astronomy*, Cambridge University Press, Cambridge, United Kingdom, 1999.
- [13] C. C. Wilcox, “The design of an adaptive tip/tilt mirror for adaptive optics,” Master’s thesis.
- [14] Spiricon, “Hartmann Wavefront Analyzer Tutorial,” pp. 1–16, 2000.
- [15] J. J. Andrews, “Multiple wavefront sensor characterization with dynamic aberration control,” Master’s thesis.
- [16] R. J. Noll, “Zernike polynomials and atmospheric turbulence,” *Journal of the Optical Society of America (1917-1983)* **66**, pp. 207–211, Mar. 1976.
- [17] D. Fried, “Least-square fitting a wavefront distortion estimate to an array of phase-difference measurements,” *J. Opt. Soc. Am. A* **67**, pp. 370–378, 1976.
- [18] W. H. Southwell, “Wave-front estimation from wave-front slope measurements,” *J. Opt. Soc. Am. A* **70**, pp. 998–1006, 1980.
- [19] W. Zou and Z. Zhang, “Generalized wave-front reconstruction algorithm applied in a shack-hartmann test,” *Applied Optics* **39**, pp. 250–268, 2000.
- [20] J. C. Strikwerda, *Finite Difference Schemes and Partial Differential Equations*, Society for Industrial and Applied Mathematics, United States, 2004.
- [21] Y. W. Kwon and H. Bang, *The finite element method using MATLAB*, CRC Press, Boca Raton, Florida, 2000.
- [22] G. P. Nikishkov, “Introduction to finite element method,” *University of Aizu, Lecture Notes*.
- [23] U. of Auckland, “Fem/bem notes,”
- [24] R. J. Noll, “Phase estimates from slope-type wavefront sensors,” *J. Opt. Soc. Am. A* **68**, pp. 139–140, 1977.
- [25] M. Chang, F. Santiago, C. O. Font, Y. Luna, E. Roura, and S. Restaino, “Horizontal path propagation measurements over the sea,” *Proc. SPIE, Glasgow, UK* **5491**.

References

- [26] M. Chang, C. O. Font, F. Santiago, Y. Luna, E. Roura, and S. Restaino, “Marine environment optical propagation measurements,” *Proc. SPIE, Denver, Colorado* **5550**.
- [27] F. Santiago, M. Chang, C. O. Font, Y. Luna, E. Roura, and S. Restaino, “Horizontal path propagation measurements over the sea, technical report to the naval research laboratory,” *MR-NRL Memorandum Report* **NRL/MR/7210-04-0277**.
- [28] L. C. Andrews, R. L. . Phillips, C. Y. Hopen, and M. A. Al-Habash, “Theory of optical scintillation,” *J. Opt. Soc. Am. A* **16**, pp. 1417–1429, 1999.
- [29] M. E. Gracheva and A. S. Gurvich, “Strong fluctuations in the intensity of light propagated through the atmosphere close to the earth,” *Izv. Vyssh. Uchebn. Zaved. Radiofiz.* **8**, pp. 717–724, 1965.
- [30] D. J. Inman, *Engineering Vibration*, Prentice Hall, New Jersey, 1994.
- [31] K. G. McConnell, *Vibration Testing, Theory and Practice*, John Wiley & Sons, New York, 1995.
- [32] N. E. Huang, Z. Shen, S. R. Long, M. C. Wu, H. H. Shih, Q. Zheng, N. Yen, C. C. Tung, and H. H. Liu, “The empirical mode decomposition and the hilbert spectrum for nonlinear and non-stationary time series analysis,” *The Royal Society* **454**, pp. 903–995, 1996.
- [33] M. Chang, E. Roura, C. Font, C. Gilbreath, and E. Oh, “Applying the Hilbert-Huang decomposition to horizontal light propagation C_n^2 data,” in *Advances in Stellar Interferometry. Proceedings of the SPIE, Volume 6268, pp. (2006).*, jul 2006.
- [34] C. Font, M. Chang, E. Oh, and C. Gilbreath, “Humidity contribution to the refractive index structure function C_n^2 ,” in *Atmospheric Propagation III. Proceedings of the SPIE, Volume 6215,(2006).*, jun 2006.
- [35] M. Born and E. Wolf, *Principles of Optics*, Cambridge University Press, Cambridge, United Kingdom, 1999.
- [36] C. Wilcox, J. R. Andrews, S. Restaino, T. Martinez, F. Santiago, E. Roura, S. Teare, and D. Payne, “Measuring a deformable mirror’s surface while under physical vibration,” *Proceedings of the IEEE Aerospace Conference* .
- [37] C. Wilcox, F. Santiago, J. R. Andrews, S. Restaino, T. Martinez, E. Roura, S. Teare, and D. Payne, “Measuring a deformable mirror’s surface while under

References

- physical vibration,” *SPIE Advanced Wavefront Control: Methods, Devices, and Applications* .
- [38] S. Restaino, T. Martinez, J. R. Andrews, C. Wilcox, F. Santiago, R. Romeo, and R. Martin, “Ultra-light weight telescope coupled with portable AO system for laser communications applications,” *SPIE Free-Space Laser Communication Technologies* **6105**.
- [39] J. J. Andrews, F. E. Penado, S. T. Broome, C. Wilcox, S. Restaino, T. Martinez, S. W. Teare, and F. Santiago, “Multiple wavefront sensor characterization with dynamic aberration control,” *New Mexico Institute of Mining and Technology* .
- [40] F. Roddier, “The effects of atmospheric turbulence in optical astronomy,” *Progress in Optics XIX* .
- [41] J. Dunphy and J. Kerr, “Scintillation measurements for large integrated-path turbulence,” *J. Opt. Soc. Am.* **63**, pp. 981–986, 1973.
- [42] R. L. Phillips and L. C. Andrews, “Measured statistics of laser-light scattering in atmospheric turbulence,” *J. Opt. Soc. Am.* **71**, pp. 1440–1445, 1981.
- [43] W. R. Coles and R. G. Frehlich, “Simultaneous measurements of angular scattering and intensity scintillation in the atmosphere,” *J. Opt. Soc. Am.* **72**, pp. 1042–1048, 1982.
- [44] D. L. Fried, “Optical resolution through a randomly inhomogeneous medium for very long and very short exposures,” *J. Opt. Soc. Am.* **56**, pp. 1372–1379, 1966.
- [45] J. W. Goodman, *Statistical Optics*, John Wiley & Sons, New York, 1985.
- [46] C. Y. Young, A. J. Masino, F. E. Thomas, and C. J. Subich, “The wave structure function in weak to strong fluctuations: an analytic

References

- model based on heuristic theory,” *Waves in Random Media* **14**, pp. 75–96, 2004.
- [47] A. S. Gurvich and M. A. Kallistratova, “Experimental study of the fluctuations in angle of incidence of a light beam under conditions of strong intensity fluctuations,” *Radiophys. Quantum Electron.* **11**, pp. 66–71, 1968.
- [48] R. J. Hill and S. F. Clifford, “Modified spectrum of atmospheric temperature fluctuations and its application to optical propagation,” *J. Opt. Soc. Am.* **68**, pp. 892–899, 1978.
- [49] S. M. Flatté, G. Wang, and J. Martin, “Irradiance variance of optical waves through atmospheric turbulence by numerical simulation and comparison with experiment,” *J. Opt. Soc. Am. A* **10**, pp. 2363–2370, 1993.
- [50] W. H. Press, S. A. Teukolsky, W. T. Vetterling, and B. P. Flannery, *Numerical Recipes in C++*, Cambridge University Press, Cambridge, United Kingdom, 2002.
- [51] W. A. Strauss, *Partial Differential Equations, An Introduction*, John Wiley & Sons, New York, 1992.
- [52] S. R. Restaino, “High angular resolution, class notes,” *University of New Mexico, Class notes* .
- [53] E. A. Roura, “Wavefront reconstruction using finite element methods,” *University of Puerto Rico, RUM, Optics Lab internal paper* .
- [54] S. Restaino, T. Martinez, J. Andrews, F. Santiago, S. Teare, and D. Payne, “MEMs and LC for compact AO systems,” *Proceedings of the. 2005 AMOS Conference* .
- [55] S. R. Restaino, C. C. Wilcox, J. R. Andrews, T. Martinez, F. Santiago, S. Teare, R. Romeo, R. Martin, and D. M. Payne, “16 inch

References

OTA prototype project at the naval research laboratory,” *Proceedings of the. 2005 AMOS Conference* .